Master Thesis

One-step dry coating of hybrid ZnO–WO_3 nanosheet photoanodes for photoelectrochemical water splitting with composition-dependent performance

University of Ulsan

School of Mechanical Engineering

MUHAMMAD SHEHROZE MALIK

January 2024

광전기화학적 물 분해를 위한 하이브리드 $ZnO-WO_3$ 나노시트 광전극의
조성에 따른 성능에 대한 건식 코팅 연구

One-step dry coating of hybrid $ZnO–WO_3$ nanosheet photoanodes for photoelectrochemical water splitting with composition-dependent performance

지도교수 천두만

이논문을 공학석사 학위 논문으로 제출함

2024 년 01 월

울산대학교 대학원 기계공학과

MUHAMMAD SHEHROZE MALIK

One-step dry coating of hybrid ZnO–WO_3 nanosheet photoanodes for photoelectrochemical water splitting with composition-dependent performance

A Thesis

Submitted to the School of Mechanical Engineering and the Graduate
School of the University of Ulsan, Republic of Korea in partial
fulfillment of the requirements for *the degree of Master of Science in
Mechanical Engineering*

By

MUHAMMAD SHEHROZE MALIK

This certifies that the thesis of Muhammad Shehroze Malik has been approved.

Thesis Committee Chairman **Professor Yoon Ho Lee**

Thesis Committee Member **Professor BoHung Kim**

Thesis Committee Member **Professor Chun Doo Man**

The Graduate School
University of Ulsan
January 2024

TABLE OF CONTENT

ACKNOWLEDGEMENTS

I would like to express my deepest gratitude to my advisor, Professor Doo-Man Chun, for his great support, and guidance and for providing me with an excellent atmosphere for doing research. I am a novice in conducting research. I can learn how to conduct research from him with his constant supervision. It is a great understatement to say that this work would not have been accomplished without his help. I thank him for his excellent effort and patience with me to train me.

My sincere thanks to my colleagues in the hybrid manufacturing technology laboratory, especially Dr. Ahmed Galal & Mr. Deepto, who supported me a lot from the beginning of my journey. The outstanding friendly nature inside the laboratory helps me incredibly to do research.

Best regards,

Malik Muhammad Shehroze

January 2024

Ulsan, South Korea

ABSTRACT

In this study, the potential of zinc oxide (ZnO), tungsten oxide (WO_3), and their composites ($ZnO–WO_3$) as photoanodes for photoelectrochemical (PEC) water splitting was investigated. $ZnO–WO_3$ nanocomposites (NCs) were deposited on fluorine-doped tin oxide substrates at room temperature using a one-step dry coating process, the nanoparticle deposition system, with no postprocesses. The hybridization composition of $ZnO–WO_3$ NCs was optimized to improve the efficiency of the PEC water-splitting reaction kinetics. The transformation of the microsized particle nanosheets (NS) powder into nanosized particle nanosheets (NS) across all photoanodes was revealed by surface morphology analysis. Diffuse reflectance and photoluminescence emission spectroscopy were employed to investigate the optical characteristics of the $ZnO–WO_3$ photoanodes. Of all the hybrid photoanodes tested, the photoanode containing 10 wt.% WO_3 exhibited the lowest bandgap of 3.20 eV and the lowest emission intensity, indicating an enhanced separation of photogenerated carriers and solar energy capture. The photoelectrochemical results showed a 10% increase in the photocurrent with increasing WO_3 content in $ZnO–WO_3$ NCs, which is attributed to improved charge transfer kinetics and carrier segregation. The maximum photocurrent recorded vs. the reversible hydrogen electrode (RHE) was 0.133 $mA{\cdot}cm^{-2}$ @ 1.23V. The observed improvement in photocurrent was nearly 22 times higher than pure WO_3 nanosheets and 7.3 times more than that of pure ZnO nanosheets, indicating the composition-dependence of PEC performance, where the synergy requirement strongly relies on utilizing the optimal $ZnO–WO_3$ ratio in the hybrid NCs.

Keywords:

$ZnO–WO_3$ hybrid photoanodes; Charge transfer kinetics; Photoelectrochemical water splitting; Nanoparticle deposition system (NPDS); Nanosheets; Nanocomposites; Bandgap optimization.

LIST OF TABLES

LIST OF FIGURES

LIST OF ABBREVIATIONS

S. no	Short Form	Full Form
1	NPDS	Nano-particle deposition system
2	SoD	Stand-off distance
3	ZnO	Zinc oxide
4	WO_3	Tungsten trioxide
5	FTO	Fluorine doped tin oxide
6	XRD	X-Ray Diffraction
7	SEM	Scanning Electron Microscope
8	XPS	X-Ray Photoelectron Spectroscopy
9	DRS	Diffuse Reflectance Spectroscopy

10	PL	Photoluminescence
11	NCs	Nanocomposites
12	NSs	Nanosheets
13	M-S	Mott–Schottky
14	V_{fb}	Flat band potential
15	N_d	Donor density concentration
16	W_{scl}	Space charge layer width
17	J_{ph}	Photoresponse current
18	IPCE	Incident photon conversion efficiency
19	R_{ct}	Charge transfer resistance
20	RHE	Reversible hydrogen electrode

CHAPTER 1

INTRODUCTION

1.1. Introduction to Photoelectrochemical (PEC) water splitting

Photoelectrochemical (PEC) water splitting is a promising technique that involves the direct conversion of sunlight and water into electricity and hydrogen as shown in **Figure. 1**. This method is notably regarded as a simple, economical, and direct energy conversion route toward a sustainable, clean, and green society [1–3]. Presently, a major source of energy (80%) on earth comes from fossil fuels, such as oil, natural gas, and coal, which are rapidly depleting and unsustainable, resulting in a drastic change in climate via global warming and other forms of pollution. Therefore, it has become necessary to shift toward green, renewable, and environmentally friendly energy sources such as solar, wind, and geothermal energy to meet the global energy demand while minimizing environmental impact and cost [4,5].

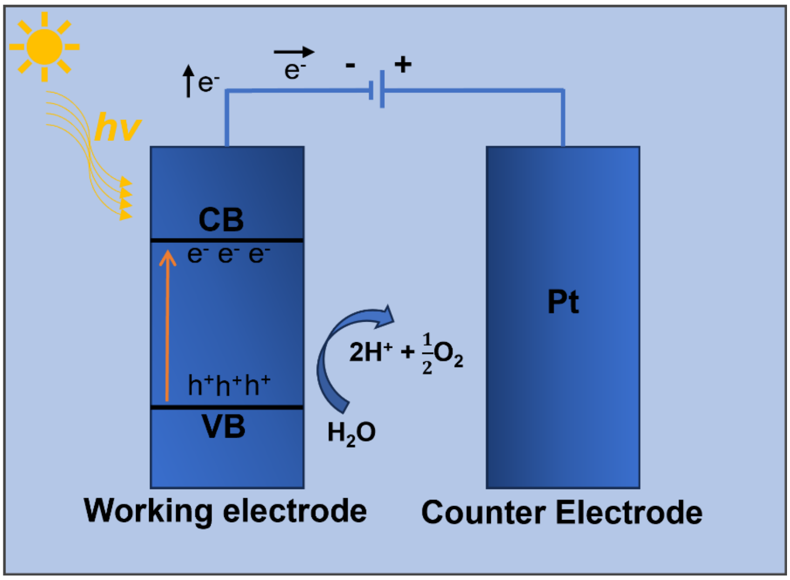

Figure 1. Principle of Photoelectrochemical water splitting.

1.2. Previous trends in photocatalysis research

Significant efforts have been made to advance metal oxide photoanodes (ZnO, TiO_2, WO_3, Fe_2O_3, and $BiVO_4$) [3,6–11], particularly in heterostructured electrode forms, to improve system performance. However, satisfying all the requirements of a PEC water-splitting system with a single semiconductor is difficult [12,13]. Fundamentally, four crucial steps determine the overall performance: (a) light absorption and charge carrier generation, (b) charge separation, (c) transporting of charges, and (d) extracting the charge carrier [14].

1.3. Strategies to improve photocatalytic activity

In this study, efforts have been made to develop heterojunction–based nanocomposites (NCs) photoanodes to obtain an improved configuration for practical PEC applications as shown in **Figure. 2**. We incorporated two semiconductors with different bandgaps, ZnO (bandgap = 3.35 eV) [15] and WO_3 (bandgap = 2.6 eV) [16], which were deposited using a nanoparticle deposition system (NPDS) [15,17]. Zinc oxide (ZnO) has emerged as the most widely used metal oxide for photoanode semiconductor applications because of its multifaceted advantages. These include cost-effectiveness, favorable bandgap, elevated electron mobility (bulk mobility: 200 $cm^2 \cdot V^{-1} \cdot s^{-1}$), increased catalytic activity, eco-friendliness, and other beneficial attributes [18]. Nevertheless, the ability of ZnO to absorb light in the visible–infrared spectrum is considerably limited by its wide bandgap (∼3.35 eV) [19]. To address this limitation, the incorporation of ZnO with a narrow-bandgap semiconductor material is a promising strategy for extending the range of light absorption. Therefore, narrow-bandgap tungsten trioxide is an emerging candidate with excellent properties such as high electron mobility, photostability, and a long hole-diffusion length (~150 nm) that can broaden the light visible absorbance range of ZnO [20].

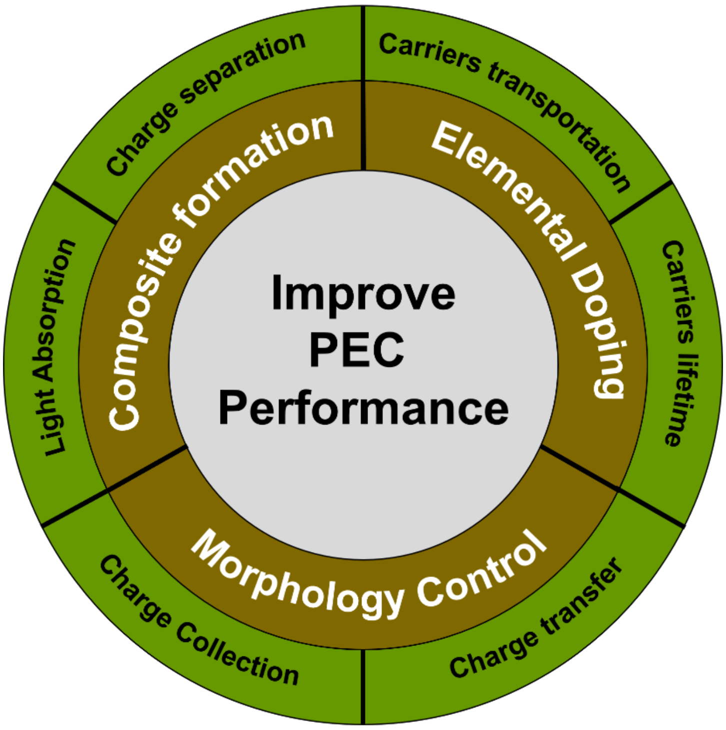

Figure 2. Optimization and modulation strategies for improving PEC performance.

1.4. Techniques for thin film fabrication

So far, vast efforts have been concentrated on the preparation of hybrid heterostructured photoanodes to achieve a lower bandgap, efficient segregation of photogenerated electron-hole pairs due to appropriate band alignment, and enhanced photoresponse current. D. Barreca et al. [6] prepared ZnO–WO_3 nano heterostructures using a multistep vapor phase process. First, ZnO samples were prepared within a reservoir using a 3 h thermal treatment at 550 °C. Second, ZnO was mixed with the WO_3 layers under optimized conditions: pressure = 0.3 M bar and RF power = 20 W for 3 h. The obtained ZnO–WO_3 composites achieved a 0.055 $mA{\cdot}cm^{-2}$ photocurrent @0.8 V vs. Ag/AgCl in 0.5 M Na_2SO_4. Y. Xu et al. [21] prepared ZnO thin films by hydrothermal synthesis at 95 °C for 4 h. WO_3 was then deposited on the prepared ZnO samples using magnetron sputtering at 1Pa ambient air pressure and 65 W RF sputtering power. The ZnO–WO_3 composites obtained in his research achieved a photocurrent of 0.353 mA/cm^2@ 0.3 V vs. Ag/AgCl in 0.5 M Na_2SO_4 solution. J. Ji et al. [22] prepared WO_3–$BiVO_4$–ZnO using different steps. Tungstic acid and polyvinyl alcohol solution were dissolved to produce a 0.12 M WO_3 precursor solution. Then annealed the solution for 1 h at 500 °C. The same procedure was repeated for $BiVO_4$ on the WO_3 film to obtain WO_3/$BiVO_4$ films. Finally, a ZnO solution was prepared and deposited onto the WO_3/$BiVO_4$ films using spin coating. In this study, the obtained WO_3–$BiVO_4$–ZnO composite at 1.23 V vs. the RHE exhibited a photocurrent of 0.190 mA/cm^2 in 0.5 M Na_2SO_4 electrolyte.

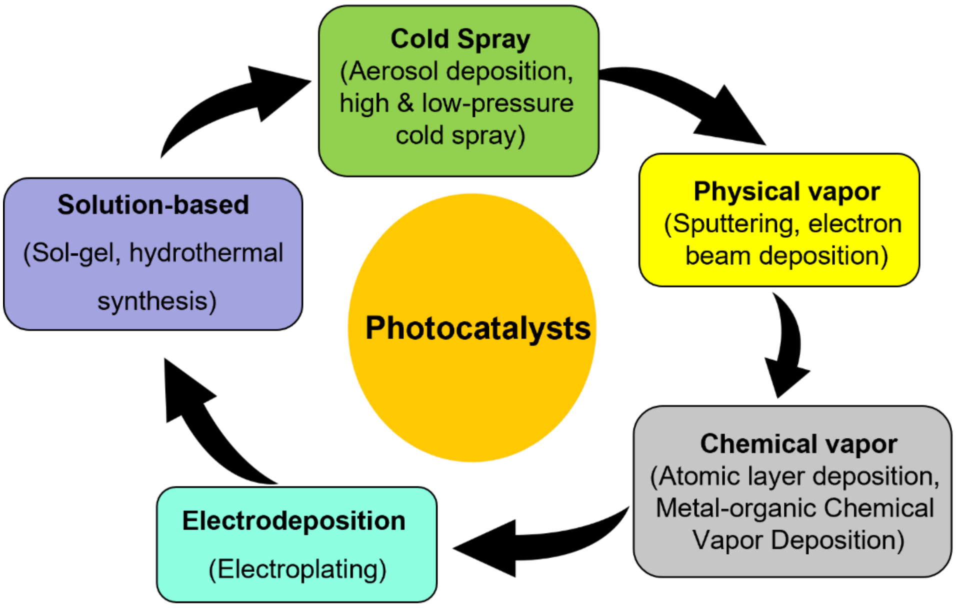

Figure 3. Fabrication techniques to improve photocatalytic performance.

The studies described above focusing on the combination of WO_3 and ZnO to produce heterostructure photoanodes show good performance in neutral electrolytes toward PEC water splitting. However, these synthesis techniques can only be used for small substrates and are limited to research and development, not commercial use. These include several reasons: (a) the considerable time required for fabricating small-sized electrodes through multiple steps to achieve the required nanosized powder, followed by its deposition onto substrates; (b) the use of dangerous reactant chemicals that produce useless toxic secondary products as waste; (c) the difficulty in scaling-up for commercial applications because of the time-consuming above techniques. In comparison, NPDS has distinct features such as; (a) one-step dry coating using the vacuum kinetic spray process at room temperature; (b) no hazardous chemicals or waste; (c) facile production of sizable electrodes for mass manufacturing in a convenient manner; (d) binder-free; and (e) no additional drying process [23,24].

1.5. Objectives of our Research

In the present study, the NPDS was used to fabricate ZnO-WO_3 hybrid photoanodes at different WO_3 contents (5, 10, 15, and 20 wt.%) on fluorine-doped tin oxide (FTO) substrates. The deposition process involved the localized and spontaneous fragmentation of microsized powder to nanosized thin films at room temperature and low vacuum conditions. The modified working electrodes with ZnO-WO_3 hybrid NCs were utilized as photoanodes for the PEC water-splitting process in a neutral medium. Our study systematically explored the impact of varying tungsten oxide (WO_3) weight ratio on the charge transfer kinetics, bandgap engineering, and the efficiency of photogenerated charge carriers' separation. The present study research outcomes demonstrate the composition-dependent PEC performance of ZnO–WO_3 hybrid photoanodes, which need to be optimized to improve the overall performance for real-life applications. The prepared electrodes were used as photoanodes in the process of PEC water splitting under neutral conditions.

The objectives of our research are:

1. Metal oxide semi-conductors based heterostructure formation through NPDS to fabricate photoanodes for optimum conditions for photoelectrochemical water splitting.
2. Composition ratio study effect to improve photoelectrochemical water splitting performance.
3. Understanding the surface morphology of fabricated heterostructures for improved photoelectrochemical water splitting.

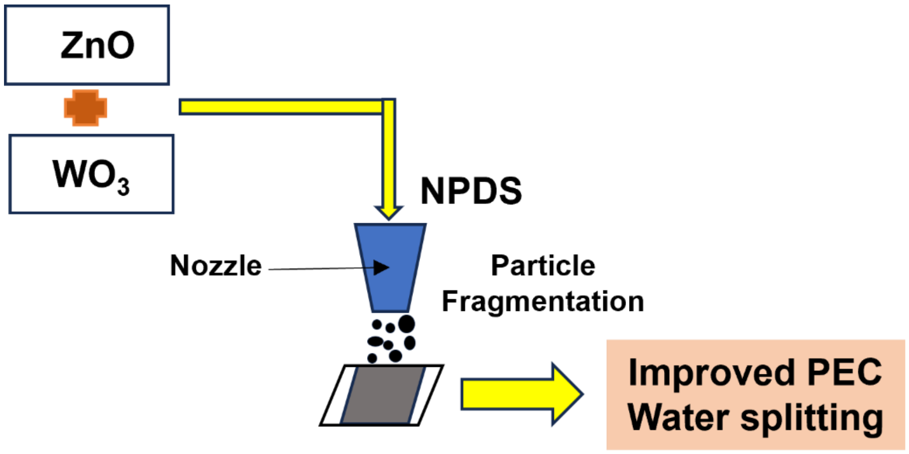

Figure 4. Objectives of the research

CHAPTER 2

Experimental Section

2.1. Material details

Microsized ZnO powder (<5 µm particle size, 99.9%, CAS # 1314–13–2, Sigma–Aldrich, USA) and WO_3 microsized powder (≤25 µm, ≥ 99% trace metals basis, CAS # 1314–35–8, Sigma–Aldrich, USA) were used to fabricate ZnO–WO_3 nanocomposites on a 2.3 mm-thick FTO (100 x 100 mm^2, surface resistivity = 7 Ω/sq, Sigma–Aldrich, USA). A 0.5 M Na_2SO_4 solution electrolyte was used as an agent with pH 6.8 (CAS# 7757–83–7, Duksan, Korea) for the investigation of PEC water splitting.

2.2. Dry coating of ZnO–WO_3 thin films by NPDS

Nanostructured ZnO–WO_3 thin films with varying WO_3 (5%, 10%, 15%, 20%) were deposited on FTO by one-step vacuum kinetic spray process, NPDS. The NPDS comprises an air compressor that supplies high pressure, a cylindrical piston known as a powder feeder, a vacuum pump, a nozzle, a controller, and a pressure chamber. The pressure was adjusted through the controller, and the microsized dry powder was mixed using a ball mill filled with a powder feeder that moved the powder to the powder chamber, where a rotating brush drives the powder and high-speed air pressure from the air compressor enters the nozzle. The powder was sprayed onto the substrate using a converging–diverging nozzle at room temperature as shown in **Figure. 5**. The impact of high-speed powder particles and the incident angle of the FTO substrate fractured the microsized powder into a nanosize range [25].

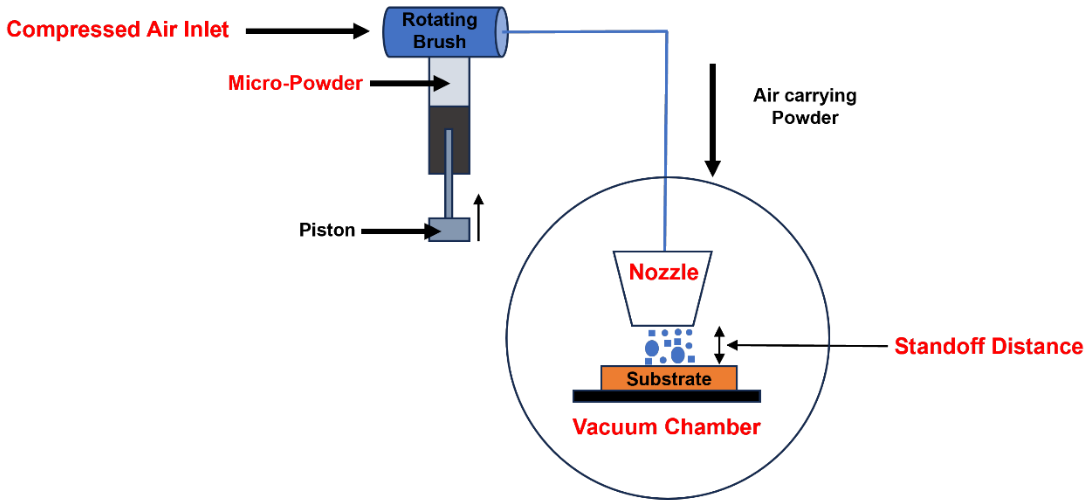

Figure 5. Deposition of nanostructured zinc–oxide–tungsten oxide hybrid photoanodes using nanoparticle deposition system.

The conditions for deposition were set as follows in **Table 1**. The fabrication time for 40 x 10 mm^2 samples using simple scanning and vacuum was less than 30 min. After deposition, there was no postprocessing.

Table 1. Process parameters for ZnO & WO$_3$ on FTO substrate.

Process Parameters	
Powder pressure (bar)	3.0
Standoff distance (mm)	3
Piston speed (rpm)	1600
Chamber pressure (bar)	0.5
Brush speed (rpm)	8000

2.3. Photoelectrochemical water splitting characteristics

An electrochemical workstation (Model: C350, Wuhan Corr-Test Instruments Corp. Ltd., China) and the solar stimulator (model: 10500, Milford, USA) with 100 mW/cm^2 power density were used in a three-electrode setup to evaluate ZnO–WO_3 NCs in 0.5 M Na_2SO_4 electrolytic solution. ZnO/FTO, WO_3/FTO, and ZnO/WO_3/FTO hybrid photoanodes with varying WO_3 content were used as the working electrodes. The counter electrode was platinum (Pt) with a mesh area of 1 x 1 cm^2, and the reference electrode was Hg/HgO in 0.5 M Na_2SO_4 electrolyte solution. Linear sweep voltammetry (LSV) profiles were examined within the potential range of −0.499–1.001 vs. Hg/HgO at a scan rate of 10 mV·s^{-1}. The potential range vs. the reference electrode was then converted to the Reversible hydrogen electrode (RHE) scale using **Equation (1)** [26].

$$E_{RHE} = E^{O}_{Hg/HgO} + E_{Hg/HgO} + 0.059 * pH \qquad (1)$$

where $E^{O}_{Hg/HgO}$ is the reference electrode potential vs. SHE (0.059), pH is 6.8, and $E_{Hg/HgO}$ is the applied potential. Therefore, the LSV curves were converted to 0–1.5 vs. RHE. The charge transfer resistance (R_{ct}) was evaluated by Nyquist plot under illumination with an AC frequency of 10 mV and a frequency range of 1 MHz–0.01 Hz. Photocurrent stability was assessed through a series of chronoamperometric (CA) measurements at a DC potential of 1.23 V vs. the RHE over five full cycles under both dark and light conditions. Mott–schottky (M.S) plots were created in the dark using electrochemical impedance spectroscopy with an AC signal of 10 mV ranging from −1–0 V vs. Hg/HgO at a frequency of 1 kHz.

2.4. Material characterization

The surface morphology was examined using scanning electron microscopy (SEM, Model: S-4800) of micropowder and nanocomposites thin films. The structure of ZnO, $WO_{3,}$ and hybrid photoanodes thin films and powders were examined using X-ray diffraction (XRD, Smart Lab, Japan) with the X-ray wavelength: Cu K-alpha from diffraction angle 10^{o} to 90^{o}. The Raman spectra for micropowder and nanostructured thin films were examined using a 1 mW laser source with 532 nm excitation wavelength (Model: Alpha 300R) in the range of 200–1200 cm^{-1}. Furthermore, the bonding states within ZnO, $WO_{3,}$ and ZnO with varying WO_3 content photoanodes binding energies ranging from 0 to 1200 eV were examined using a source K-alpha X-ray photoelectron spectrometer. Photoluminescence (PL) emissions were recorded using a fluorescence spectrometer (Cary Eclipse, US) in a range of 350–600 nm wavelength. Furthermore, the optical diffuse reflectance (DRS) of nanostructured ZnO, WO_3, and ZnO–WO_3 hybrid photoanodes was measured using a (UV–Vis–NIR) spectrophotometer (Cary 5000, US) in the wavelength range of 300–699 nm.

CHAPTER 3

Characterization

3.1. XRD analysis

The crystalline structures of ZnO, WO_3, and ZnO–WO_3 mixed micron particle powders at various concentrations of 5, 10, 15, and 20 wt.% WO_3 were examined using XRD patterns (**Figure. 6(a))**. The XRD pattern of ZnO shows characteristic diffraction peaks at 31.16°, 33.82°, 35.64°, 46.96°, 56.02°, 62.3°, 65.82°, 67.42°, and 68.56°. These peaks correspond to (1 0 0), (0 0 2), (1 0 1), (1 0 2), (1 1 0), (1 0 3), (2 0 0), (1 1 2), and (2 0 1) hexagonal ZnO phase crystalline planes (space group: $P6_3mc$, 01–086–8198), respectively [27]. The microsized WO_3 powder exhibited three main diffraction peaks at 22.56°, 23.04°, and 23.82°, corresponding to (0 0 2), (0 2 0), and (2 0 0) monoclinic WO_3 phase crystalline planes (space group: $P2_{1/n}$, 00–043–1035) [28]. All mixed powders of ZnO–WO_3 showed the presence of all peaks of ZnO and WO_3, indicating the presence of both hexagonal ZnO and monoclinic WO_3 without the presence of any new hybrid structural phase because of the predeposition grinding by ball milling process [29].

Figure. 6(b) shows the XRD patterns of the bare FTO substrate and nanostructured thin films of ZnO, WO_3, and ZnO–WO_3 hybrid NCs at different WO_3 contents (5, 10, 15, and 20 wt.%) on FTO. The XRD pattern of FTO shows several peaks at 26.48°, 33.66°, 37.72°, 54.5°, 61.5°, and 65.46°. The XRD pattern of nanosized pure ZnO thin film showed peaks at 31.78°, 34.42°, 36.36°, 47.56°, 56.58°, and 62.86°, 67.94° and 69.08°. For the WO_3 thin film only major peaks are visible at 23.12°, 23.64°, and 24.38° because of its low content in the nanocomposites (NCs). It is observed that the thin film peak positions have shifted a little comparatively to powder peak positions. This is because of fracturing, shattering, and random ordering of the particles during deposition. The XRD patterns of the ZnO, WO_3, and ZnO–WO_3 NC thin films show relatively smaller peak intensities than those of the corresponding powder. This behavior is attributed to the polycrystalline nature of the nanostructured films deposited by NPDS under rough vacuum conditions during the kinetic spray process [30]. This demonstrates the fragmentation of the initial microsized particles into many domains with a small nanosize, which is accompanied by an increase in the number of defective sites. These defect states act as additional reaction sites for oxygen evolution [23].

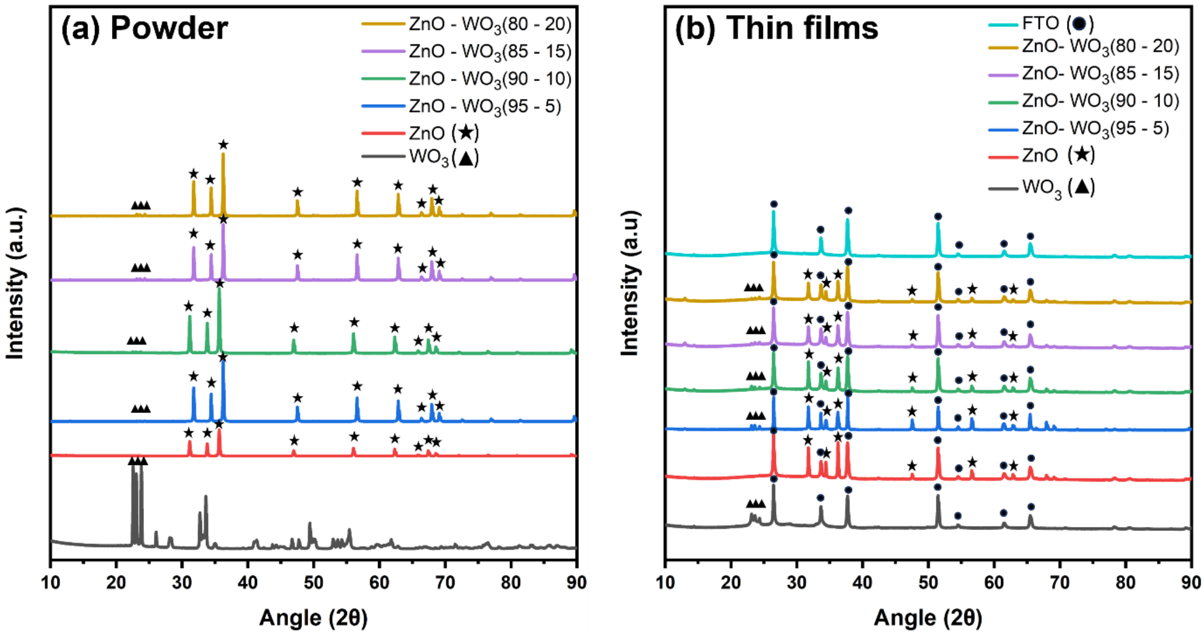

Figure 6. X-ray diffraction patterns of ZnO–WO_3 in powder-form (a), ZnO–WO_3 coated on fluorine-doped tin oxide substrate (b).

3.2. Raman spectra analysis

Raman analysis was used to confirm the crystal structure, crystal quality, and presence of both ZnO and WO_3 species in the mixed micron powder and nanostructured thin films. The Raman spectrum of the WO_3 micron powder shown in **Figure. 7(a)** reveals several distinct peaks at 275, 326, 717, and 809 cm^{-1} [31]. Raman peaks at 275 and 326 cm^{-1} correspond to the stretching and bending vibrations of the lattice oxygenated bonds (W–O), respectively [32]. Meanwhile, the observed Raman peaks at higher Raman shift values of 717 and 807 cm^{-1} increase from several stretching vibrations related to W^{VI+}–O of monoclinic crystal structure, corresponding to the stretching vibrations of the bridging oxygen [33]. The prominent peaks detected at 807, 717, and 275 cm^{-1} exhibited distinct intensities and were characteristic vibrational modes of crystalline WO_3 (monoclinic phase) [34–36]. The Raman spectrum of the ZnO powder in **Figure. 7(a)** shows several distinct peaks at 329, 380, 436, and 1154 cm^{-1}. The A_1-symmetry mode at 380 cm^{-1} represents the first-order transverse optical (TO) phonon mode [37]. The E_{2L} mode corresponds to the low-frequency vibration of oxygen atoms, whereas the E_{2H} mode corresponds to the high-frequency vibration of heavy zinc (Zn) atoms. [38]. The prominent Raman mode at 329 cm^{-1} is primarily associated with the superimposition of second order optical phonon vibration (E_{2H}–E_{2L}) [39,40]. The most prominent Raman peak at 436 cm^{-1} is related to the E_{2H} symmetry and nonpolar second order vibration of the hexagonal crystalline structure of zinc oxide [41,42]. However, 1154 cm^{-1} represents the second-order vibration mode in ZnO. Similarly, the Raman spectrum for ZnO–WO_3 (10%) mixed micron powder was observed, with all Raman peaks for WO_3 powder (275, 717, and 809 cm^{-1}) corresponding to (W–O) lattice bond and stretching vibration related to W^{VI+}–O (**Figure. 7(a))**. In addition, the peak at 326 cm^{-1} of WO_3 vanished in the ZnO–WO_3 (10%) mixed micron powder because of its proximity to the ZnO powder peak at 329 cm^{-1}. However, 1154 cm^{-1} represents the second-order vibration mode in ZnO. Similarly, the Raman spectrum for ZnO–WO_3 (10%) mixed micron powder was observed, with all Raman peaks for WO_3 powder (275, 717, and 809 cm^{-1}) corresponding to (W–O) lattice bond and stretching vibration related to W^{VI+}–O (**Figure. 7(a))**. In addition, the peak at 326 cm^{-1} of WO_3 vanished in the ZnO–WO_3 (10%) mixed micron powder because of its proximity to the ZnO powder peak at 329 cm^{-1}. However, 380, 436, and 1154 cm^{-1} peaks of ZnO powder corresponding to the first-order TO phonon mode and superimposition of second-order optical phonon vibration (E_{2H}–E_{2L}) were present in the Raman spectra of the ZnO–WO_3 (10%) powder (**Fig. 7(a)).**

Figure. 7(b) shows the Raman peaks for ZnO on the FTO substrate, indicating all peaks of the powder, which are 329, 380, and 436 cm^{-1}, without any change in peak position, demonstrating that the hexagonal structure remained the same after deposition. The main peak known as E_2 (High) at 436 cm^{-1} is the fingerprint of the wurtzite crystal structures [43]. Peaks at 275, 326, and 807 cm^{-1} for WO_3 nanostructure thin films show no change compared with powder peaks; however, the peak at 717 cm^{-1} shifted to 709 cm^{-1}, indicating poor crystalline quality and fragmentation of WO_3 particle size from micro to nano, as explained in the SEM analysis. Furthermore, for ZnO–WO_3 thin films on the FTO are shown in **Figure. 7(b)**. All hybrid thin films showed the same peaks of ZnO and WO_3. The observed peak at 275 cm^{-1} for WO_3 showed a positive shift to 278 cm^{-1} for hybrid thin films, indicating an interaction between ZnO and WO_3. However, the 717 cm^{-1} peak in the WO_3 powder shifted negatively to 709 cm^{-1}, indicating a decrease in the crystalline quality and overall fragmentation by lattice disorder, as explained in the XRD analysis.

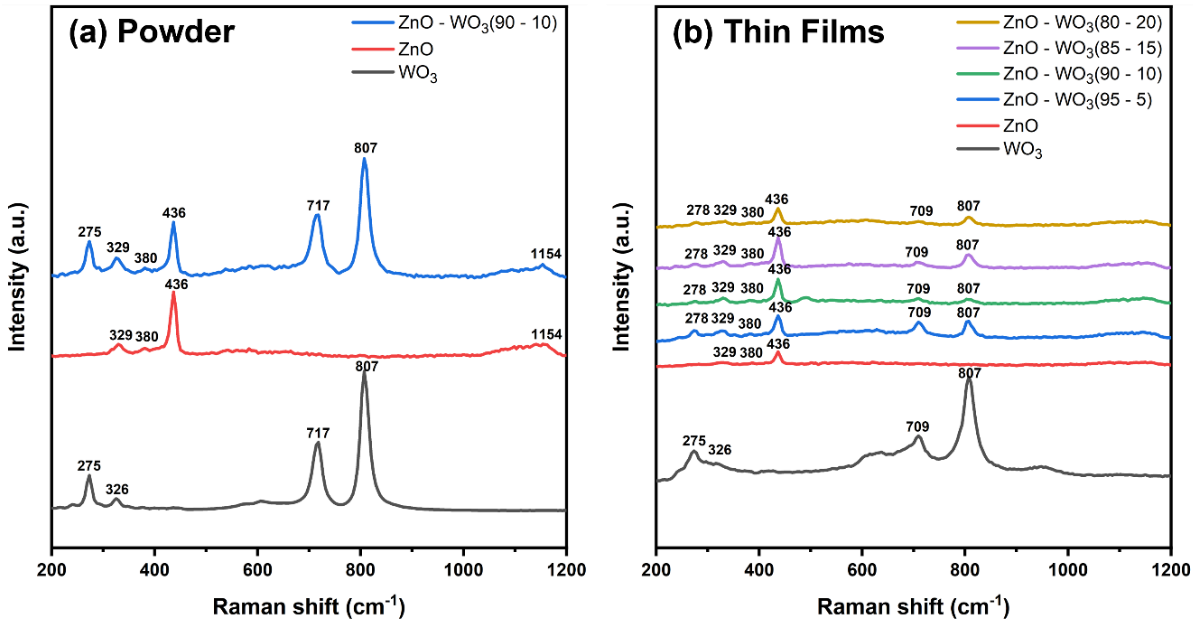

Figure 7. Raman spectra of WO_3, ZnO, and ZnO–WO_3 (10%) powders (a) WO_3, ZnO, and ZnO–WO_3 (5%, 10%, 15%, and 20%) (b) thin films on fluorine-doped tin oxide.

3.3. SEM analysis

The surface morphologies of ZnO, WO_3, and ZnO with 10% WO_3 powder were measured using SEM (**Figure. S1)**. The shapes and sizes of the ZnO and WO_3 particles were observed. The size of the WO_3 microparticle powder ranges <50 µm. However, ZnO powder showed multiple variations in sheets and rods with particles range <25 µm. Similarly, the presence of both zinc oxide and tungsten oxide particles were visible in the ball-milled ZnO–WO_3 (10%) mixture before deposition of similar sizes <25 µm and shape.

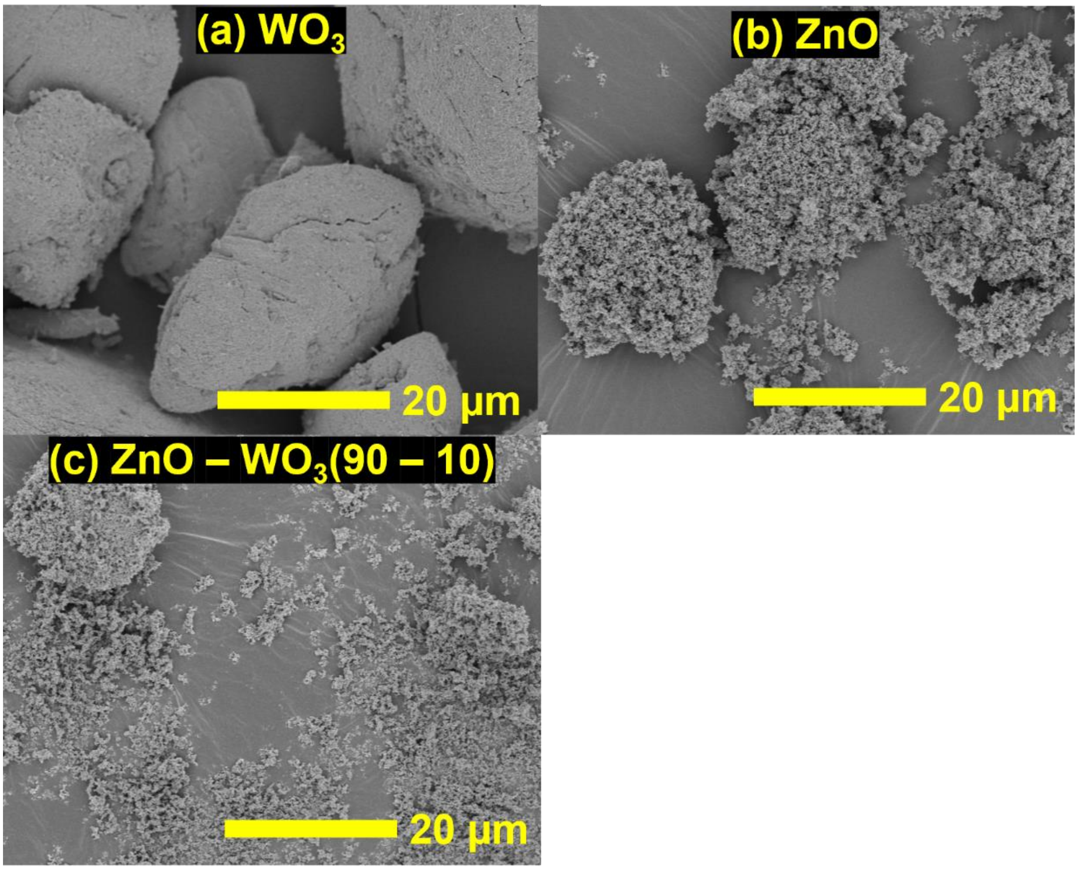

Figure 8. Scanning electron microscopy images of ZnO powder (a), WO_3 powder (b), and ZnO–WO_3 composite powder with 10% WO_3 content (c).

Figure. 9(a) shows WO_3 deposited on the FTO substrate; the particle size was significantly reduced from 25 µm to <500 nm and the SEM image showed several nanosheets. This could be due to the dispersion of the grains in each particle after deposition because of high kinetic energy or the impact between accelerated microparticles and the substrate, causing microparticles to fracture to a smaller nanosize during deposition. When a ZnO thin film was deposited on FTO, multiple variations of nanosheets and nanorods with particle sizes ranging <500 nm were observed (**Fig. 9(b)**). Therefore, large particles of ZnO and WO_3 were fragmented into smaller particles (particularly of grain size before deposition) because of the accelerated particles with high-impact energy collision with the metallic substrate (FTO) (**Fig. 8 (a,b)**). The SEM morphologies of the hybrid ZnO–WO_3 (5%, 10%, 15%, 20%) thin films are shown in **Figs. 9(c) and 10(a–c)**. All hybrid nanocomposites contain particles of similar shape and size <500 nm. An overall uniform distribution of particles is observed in the microscale micrographs of all thin films. The shift from microscale powder to nanosized particles in all NC thin films resulted in more defective sites, which acted as more reaction sites, as explained in the XRD analysis.

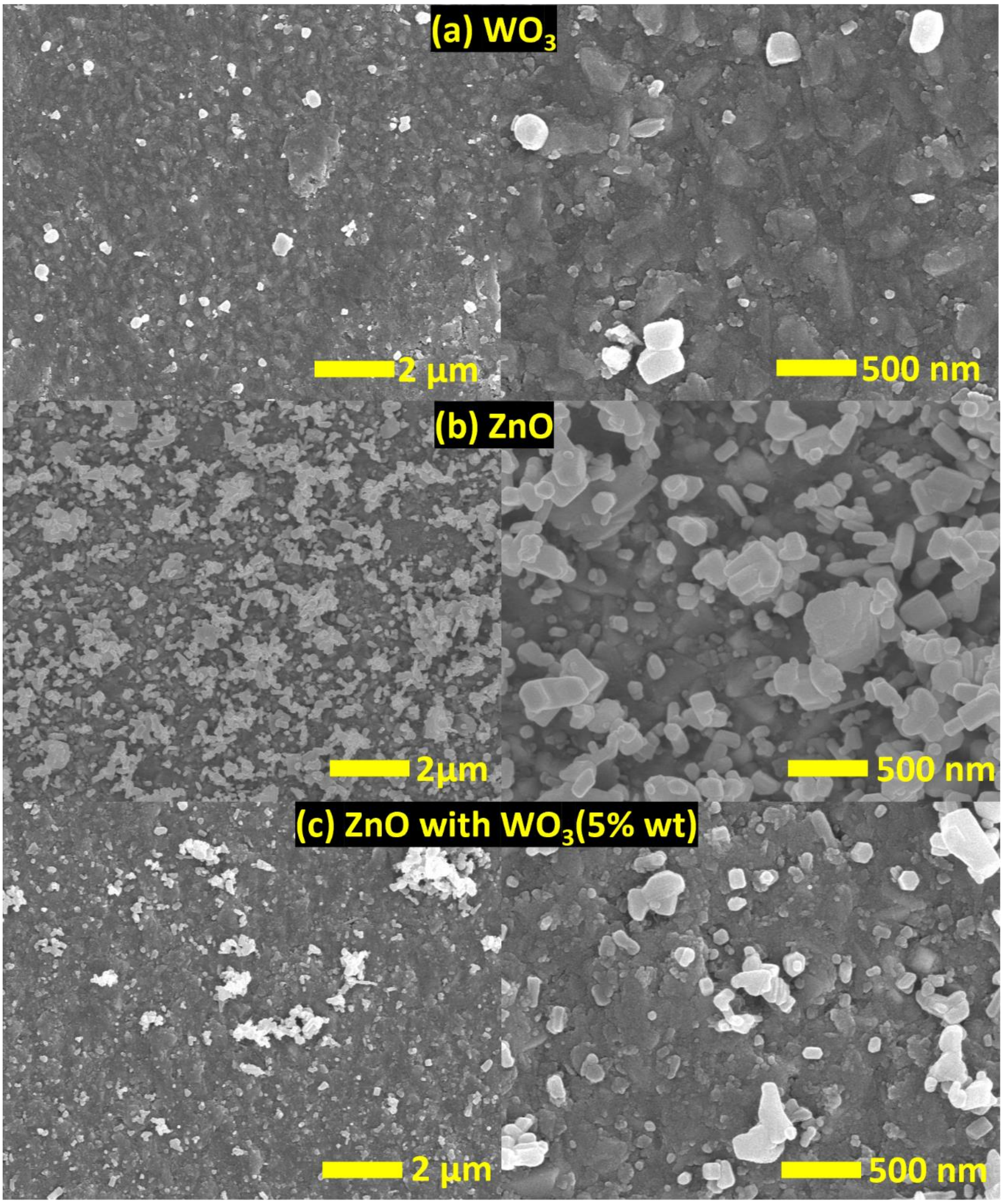

Figure 9. Scanning electron microscopy images of WO_3 (a) ZnO (b) ZnO with 5% (c) WO_3 content on fluorine-doped tin oxide.

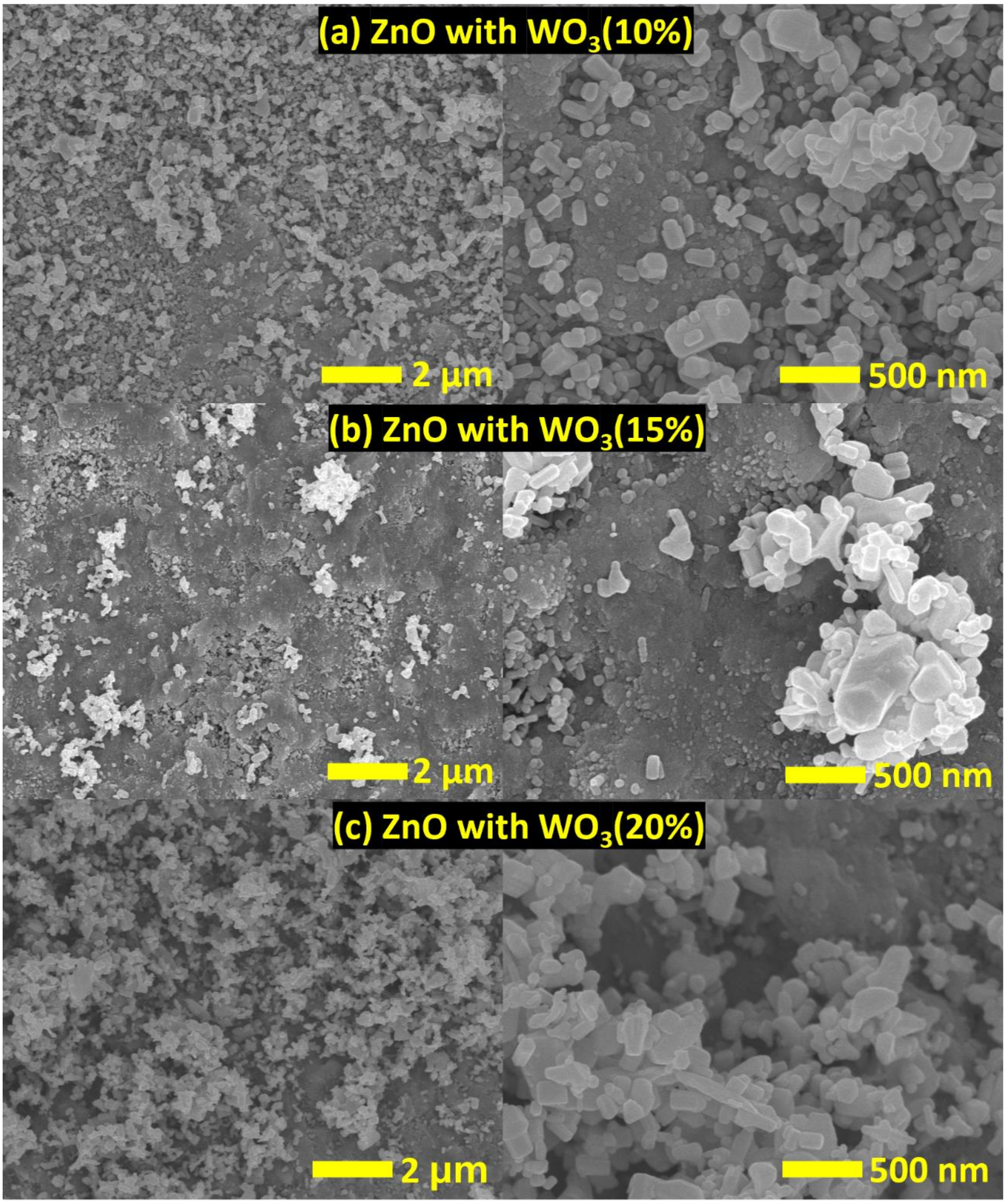

Figure 10. Scanning electron microscopy images of ZnO with 10% (d) ZnO with 15% (e) ZnO with 20% (f) WO_3 content on fluorine-doped tin oxide.

3.4. XPS analysis of ZnO–WO_3 NCs

The interfacial chemical bonding states on ZnO NSs, WO_3 NSs, and ZnO–WO_3 hybrid NCs at different WO_3 contents (5, 10, 15, and 20 wt.% WO_3) were investigated using XPS survey spectra (**Figure. 11(a)**), which revealed the presence of typical signals corresponding to Zn, W, C, Sn, and O elements. These signals were characterized by the active states of ZnO, $WO_{3,}$ and FTO from the holding substrate. The high-magnified XPS scans of W 4f, Zn 2p, and O 1s are illustrated in **Figure. 11(b–d)**.

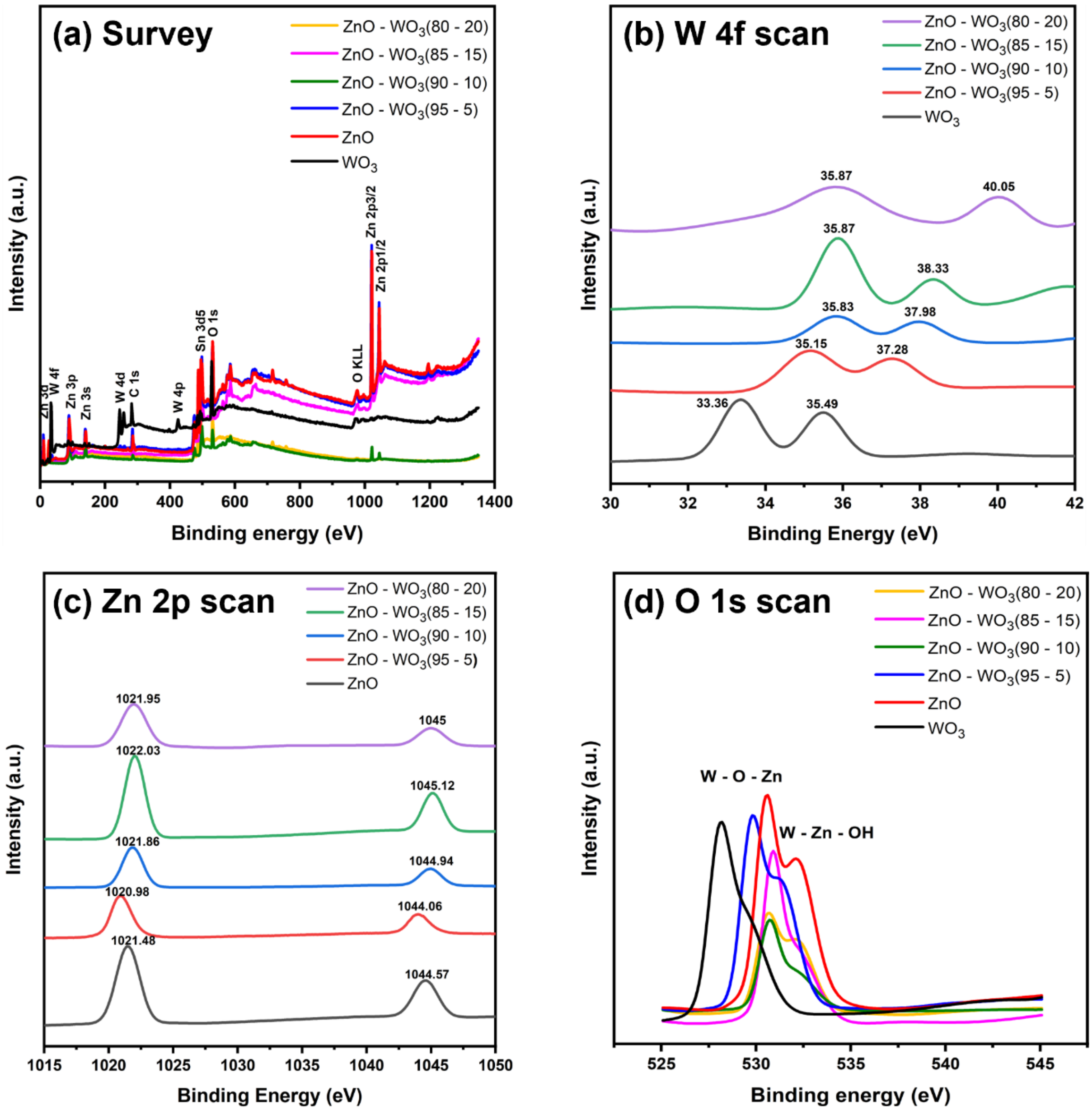

Figure 11. X-ray photoelectron spectroscopy (XPS) survey spectrum (a), high-magnified W 4f (b), Zn 2p (c), and O 1s (d) XPS scans of ZnO–WO$_3$ hybrid nanocomposites deposited on fluorine-doped tin oxide.

Fig. 12(a–e) shows the deconvolute XPS scans of the Zn 2p band for both pure ZnO NSs and ZnO–WO$_3$ hybrid NCs at various WO$_3$ contents: 5 wt.%, 10 wt.%, 15 wt.%, 20 wt.%. In the high-resolution Zn 2p XPS scan of pure ZnO NSs, two distinct subband peaks were observed, attributing to Zn 2p$_{3/2}$ and Zn 2p$_{1/2}$ at 1021.48 and 1044.57 eV, respectively. The estimated peaks in the ZnO–WO$_3$

NCs at various WO_3 contents are shown in **Table 2**. The average energy separation between Zn $2p_{3/2}$ and Zn $2p_{1/2}$ was approximately 23.09, which corresponds to the metallic Zn phases [44]. The binding energy of the deconvolute Zn 2p peaks negatively shifts with increasing WO_3 content up to 5 wt.%; however, increasing WO_3 contents (10 wt.%–20 wt.%) causes a positive shift in binding energy to a higher value than with ZnO NCs. This indicated that improving surface bonding and synergy between ZnO and WO_3 in the hybrid NCs could enhance the interfacial electron density at ZnO grain boundaries (**Table 2)**.

Table 2. Band centers deconvoluted Zn 2p, O 1s, and W 4f X-ray photoelectron spectroscopy scans of ZnO–WO_3 nanocomposite hybrid photoanodes at various WO_3 contents (wt.%).

Band	**Binding energy (eV)**					
	WO_3	**ZnO–WO_3 (80%–20%)**	**ZnO–WO_3 (85%–15%)**	**ZnO–WO_3 (90%–10%)**	**ZnO–WO_3 (95%–5%)**	**ZnO**
W 4f	33.36	35.87	35.87	35.83	35.15	-
	35.49	40.05	38.33	37.98	37.28	-
O 1s	528.04	530.56	530.83	530.66	529.72	530.49
	529.24	532.14	531.90	531.90	531.27	532.16
Zn 2p	-	1021.95	1022.03	1021.86	1020.98	1021.48
	-	1045	1045.12	1044.94	1044.06	1044.57

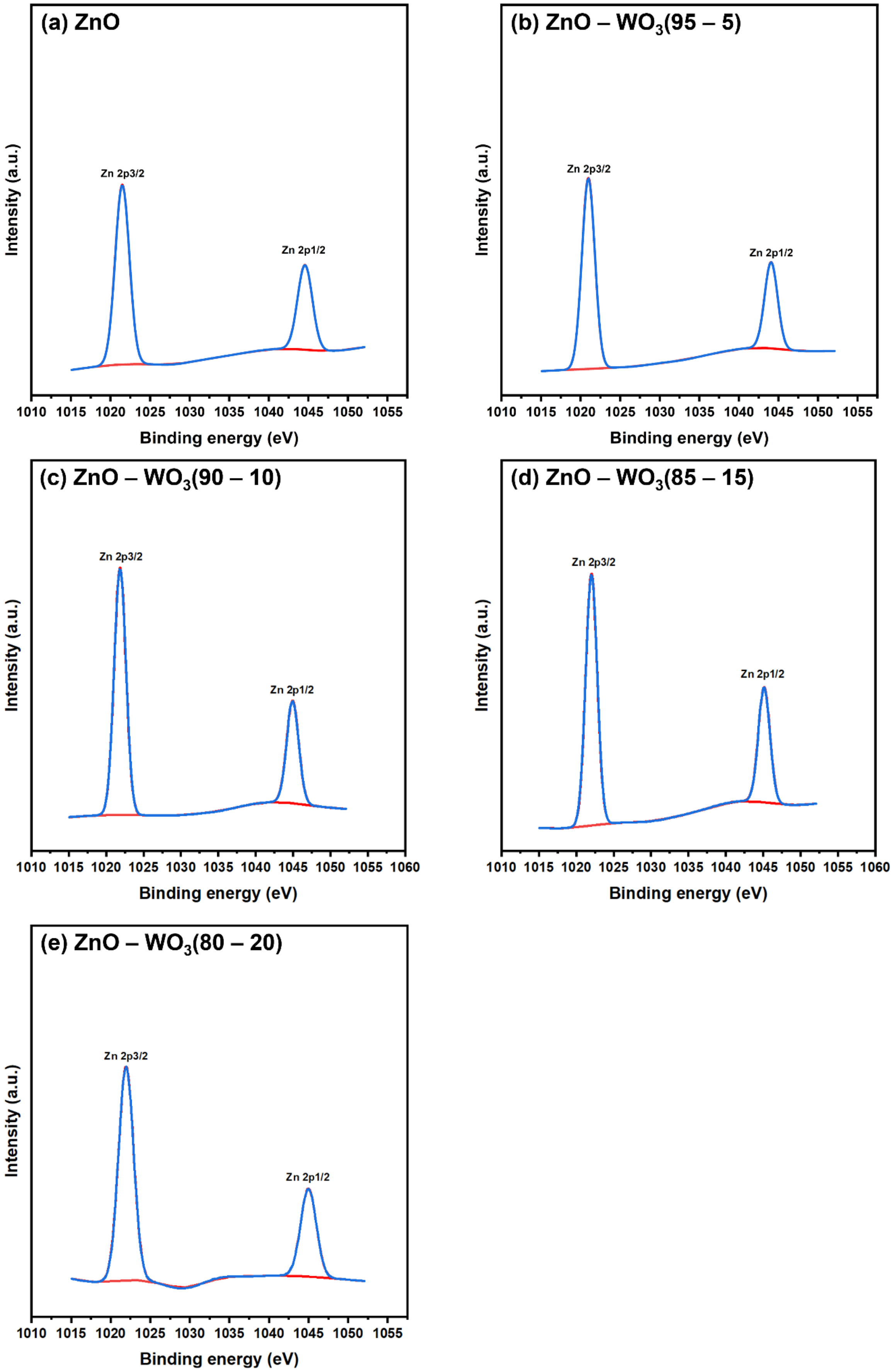
(a) ZnO
Zn 2p3/2
Zn 2p1/2
Intensity (a.u.)
1010 1015 1020 1025 1030 1035 1040 1045 1050 1055
Binding energy (eV)
(b) ZnO – WO$_3$(95 – 5)
Zn 2p3/2
Zn 2p1/2
Intensity (a.u.)
1010 1015 1020 1025 1030 1035 1040 1045 1050 1055
Binding energy (eV)
(c) ZnO – WO$_3$(90 – 10)
Zn 2p3/2
Zn 2p1/2
Intensity (a.u.)
1010 1015 1020 1025 1030 1035 1040 1045 1050 1055 1060
Binding energy (eV)
(d) ZnO – WO$_3$(85 – 15)
Zn 2p3/2
Zn 2p1/2
Intensity (a.u.)
1010 1015 1020 1025 1030 1035 1040 1045 1050 1055 1060
Binding energy (eV)
(e) ZnO – WO$_3$(80 – 20)
Zn 2p3/2
Zn 2p1/2
Intensity (a.u.)
1010 1015 1020 1025 1030 1035 1040 1045 1050 1055
Binding energy (eV)

Figure 12. Deconvoluted Zn 2p scans of ZnO NSs (a) and ZnO–WO_3 NCs with 5 wt.% (b), 10 wt.% (c), 15 wt.% (d) 20 wt.% (e) WO_3.

Figure. 13(a) shows high-resolution deconvoluted O 1s scans of WO_3 NSs with double degenerate binding states at 530.49 and 532.16 eV [45,46]. These bands showed the presence of oxygenated bonds, including internal lattice oxygen (W–O) and adsorbed water molecules (W–OH) [47]. However, the characteristic oxygenated bonds shown in **Figure. 13(b)** of ZnO were detected at 528.04 and 529.24 eV, which are attributed to Zn–O and Zn–OH, respectively [15,48]. The deconvolute O 1s scans of ZnO–WO_3 NCs at various WO_3 contents (5 –20 wt.%) are illustrated in **Figure. 13(c–f)**, and the estimated peak positions are shown in **Table 2.**

Figure. 14(a) shows deconvoluted W 4f XPS scans of pure WO_3 NSs, which demonstrated the presence of W 4f $4f_{7/2}$ at 33.36 eV and W $4f_{5/2}$ at 35.49 eV, and a small peak of $5p_{3/2}$ in WO_3 [49,50]. Furthermore, ZnO with WO_3 (5%, 10%, 15%, 20%) heterostructure thin films in all three main peaks are shown in Fig. 14(b–e), and their values are listed in **Table 2**. The heterostructure nanocomposites with different WO_3 contents showed that increasing the WO_3 content leads to a positive binding energy peak shift for both $4f_{7/2}$ and $4f_{5/2}$ peaks, demonstrating the strong coupling between WO_3 and ZnO in the deposited heterostructure films within the nanoscale range. . Additionally, this obvious positive shift can be because of the presence of interfacial charge transfer from WO_3 to ZnO in the ZnO/WO_3 heterojunction interface. When WO_3 and ZnO are combined in different compositions, the formation of heterojunctions between two semiconductors, the WO_3 semiconductor will transfer interfacial charge to the ZnO semiconductor through the formed interface, thus leading to the increase of W binding energy (**Figure 11(b)**) and the decrease of Zn binding energy. More

W content means more charge transfers. Furthermore, this is also visible in **Figure 16(b)** that the conduction band position of WO_3 is -3.35 eV above ZnO at -0.65 eV.

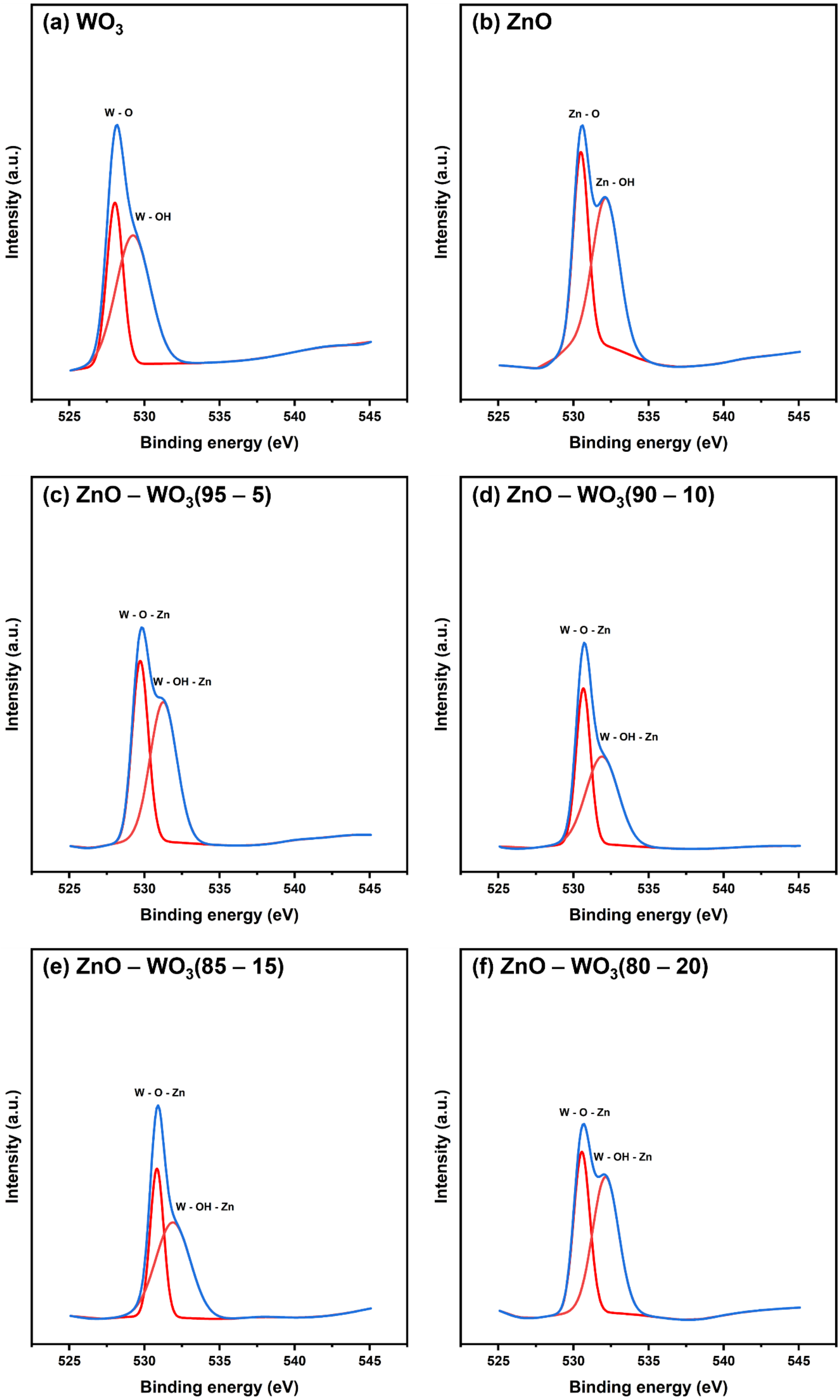
(a) WO_3
W - O
W - OH
(b) ZnO
Zn - O
Zn - OH
(c) ZnO – WO_3(95 – 5)
W - O - Zn
W - OH - Zn
(d) ZnO – WO_3(90 – 10)
W - O - Zn
W - OH - Zn
(e) ZnO – WO_3(85 – 15)
W - O - Zn
W - OH - Zn
(f) ZnO – WO_3(80 – 20)
W - O - Zn
W - OH - Zn
Intensity (a.u.)
Binding energy (eV)
525
530
535
540
545

Figure 13. Deconvoluted O 1s X-ray photoelectron spectroscopy scans of WO_3 NSs (a), ZnO NSs (b), and hybrid ZnO–WO_3 NCs at 5 wt.% (c), 10 wt.% (d), 15 wt.% (e), and 20 wt.% (f) WO_3.

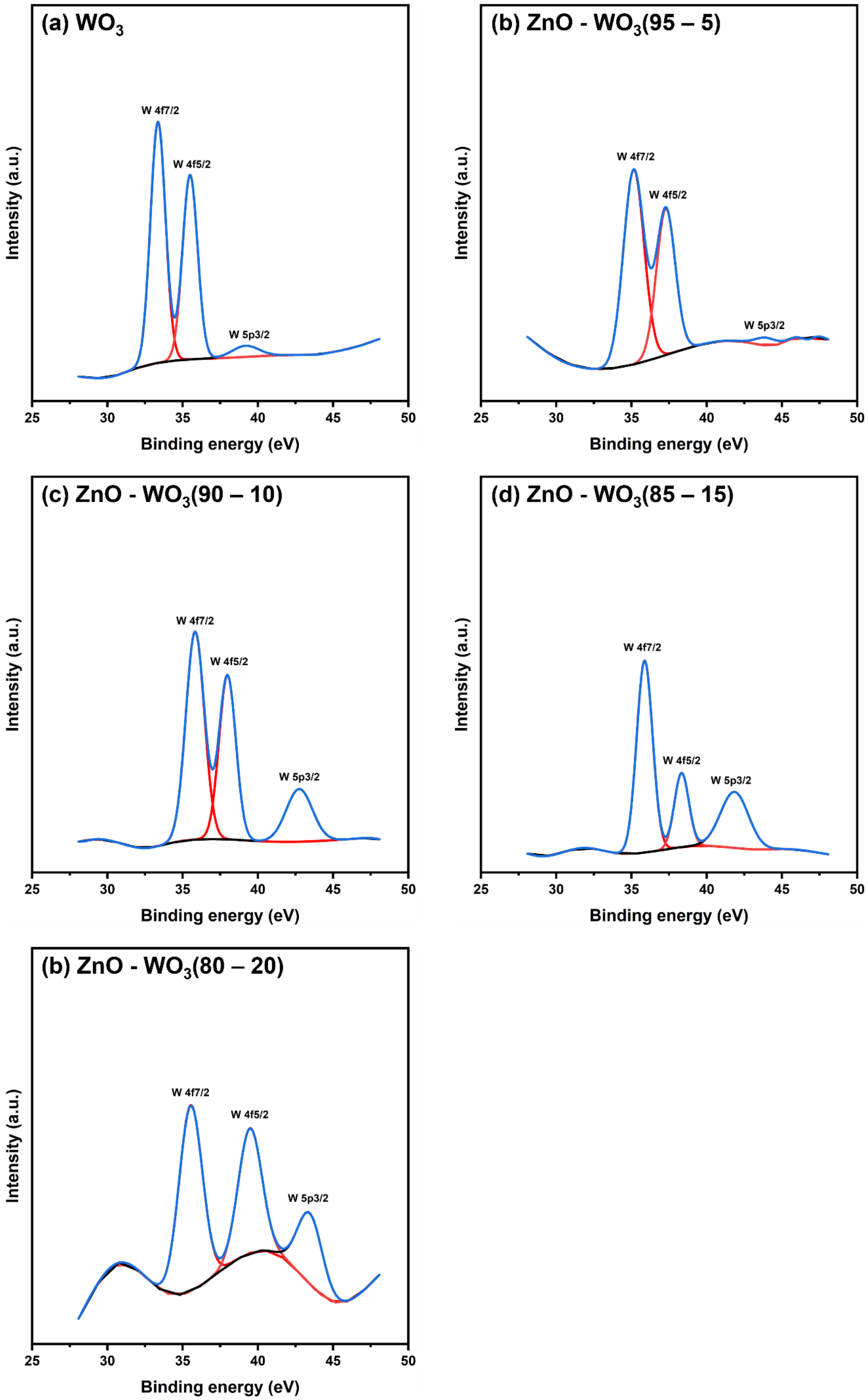
(a) WO_3
W 4f7/2
W 4f5/2
W 5p3/2
Intensity (a.u.)
Binding energy (eV)
25
30
35
40
45
50
(b) ZnO - WO_3(95 – 5)
W 4f7/2
W 4f5/2
W 5p3/2
Intensity (a.u.)
Binding energy (eV)
(c) ZnO - WO_3(90 – 10)
W 4f7/2
W 4f5/2
W 5p3/2
Intensity (a.u.)
Binding energy (eV)
(d) ZnO - WO_3(85 – 15)
W 4f7/2
W 4f5/2
W 5p3/2
Intensity (a.u.)
Binding energy (eV)
(b) ZnO - WO_3(80 – 20)
W 4f7/2
W 4f5/2
W 5p3/2
Intensity (a.u.)
Binding energy (eV)

Figure 14. Deconvoluted W 4f X-ray photoelectron spectroscopy scan of WO_3 (a), 5% WO_3 (b), 10% WO_3 (c), 15% WO_3 (d), 20% WO_3 (e) heterostructure thin films.

3.5. Analysis of optical bandgap of ZnO–WO_3 NCs hybrid

Diffuse reflectance (R%) spectroscopy was used to examine the optical properties of pure ZnO nanosheets, WO_3 nanosheets, and ZnO–WO_3 NC hybrid photoanodes at different weight ratios of WO_3 (5 wt.%, 10 wt.%, 15 wt.%, and 20 wt.%) in the wavelength range of 200–799 nm (**Figure. 15(a, b))**. Tauc's plots of ZnO–WO_3 NCs at different WO_3 contents are shown in **Figure. 15(a)**, where linear extrapolation in the high energy region provided the optical bandgap value of direct bandgap semiconductor according to **Equation (2)** [51,52].

$$\frac{\alpha}{S} = F = \frac{(1-R)^2}{2*R} \qquad (2)$$

$$(\alpha h v)^2 = C(hv - E_g) \qquad (3)$$

where α is the absorption coefficient, v is the incident light frequency, E_g is the optical bandgap energy, h is the Planck constant, C is the proportionality constant, and S is the scattering coefficient.

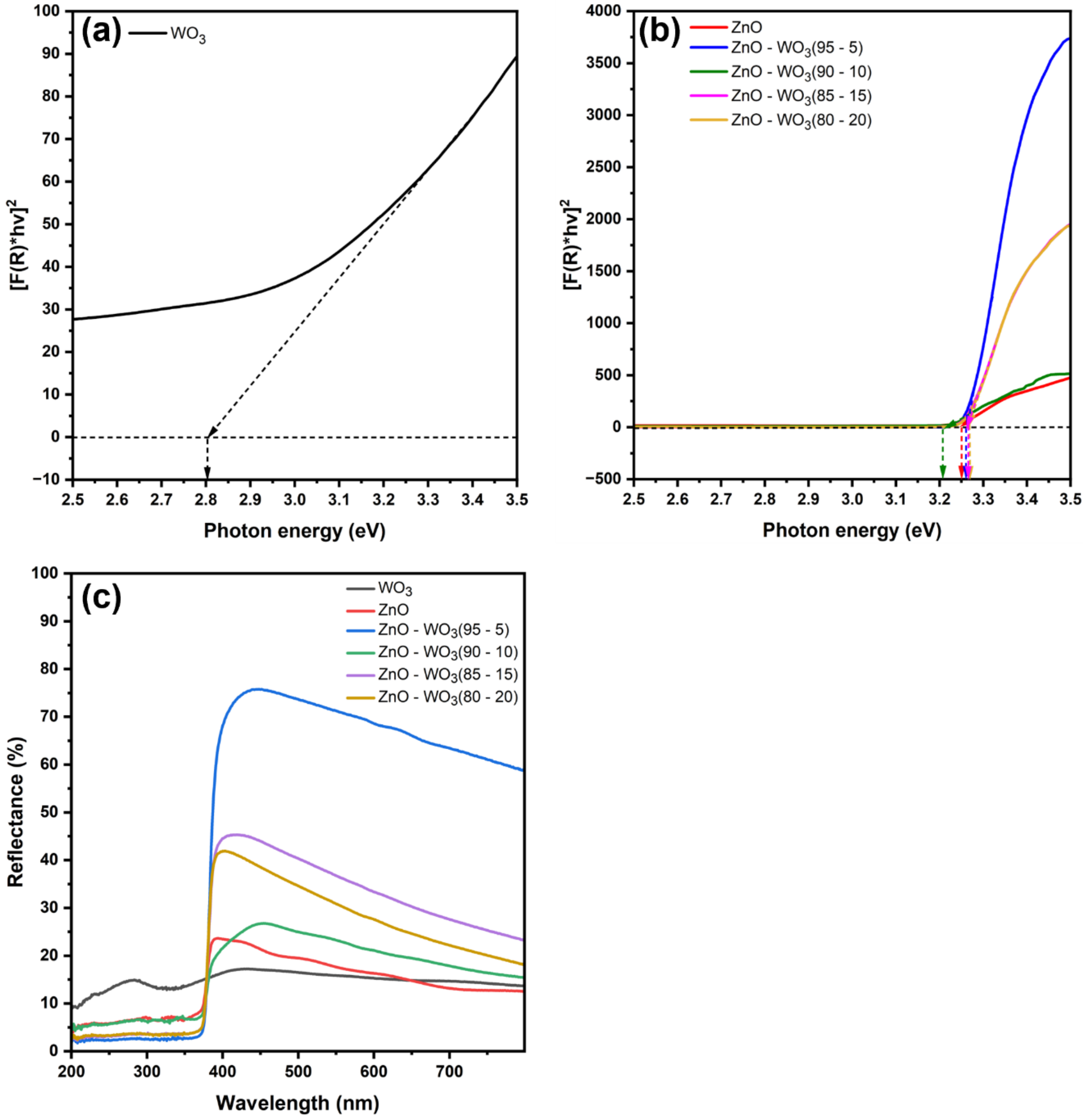

Figure 15. Ultraviolet–visible diffuse reflectance spectra (a) and the calculated Tauc's plot (b) of ZnO–WO$_3$ hybrid nanocomposites photoanodes.

The estimated E_g values of pure nanostructured thin films of WO$_3$ and ZnO are 2.8 and 3.25 eV, respectively. The incorporation of WO$_3$ into the hybrid NCs did not significantly affect the band structure of the ZnO host lattice, where the estimated E_g values in ZnO–WO$_3$ hybrid NCs at WO$_3$ ratios of 5, 10, 15, and 20 wt.% were 3.26, 3.20, 3.264, and 3.27 eV, respectively.

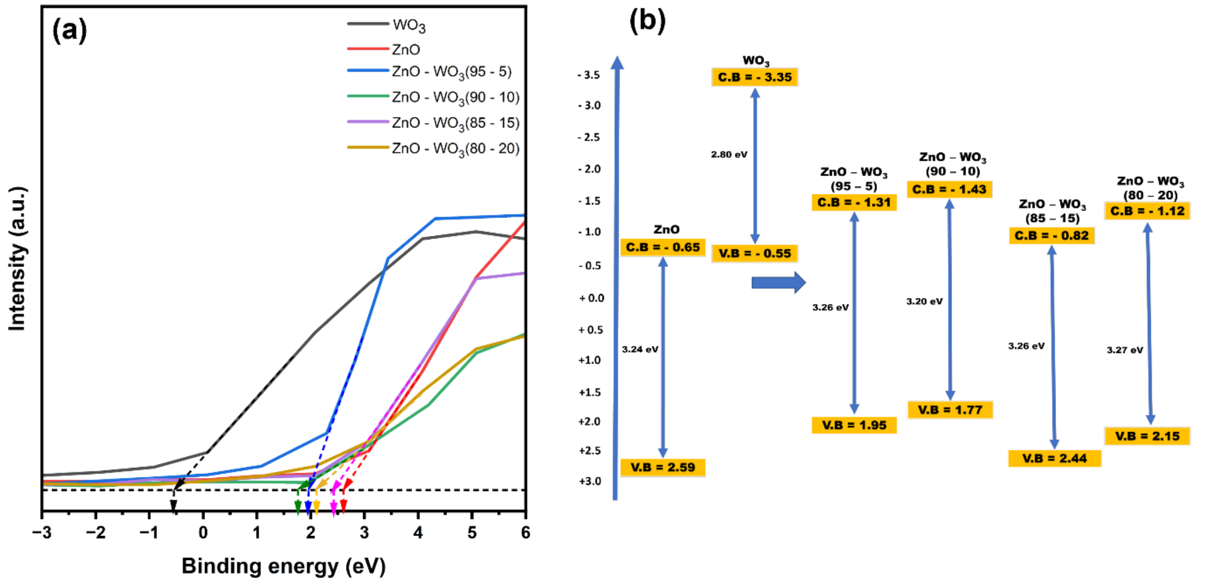

Figure 16. Valence band calculation from survey spectrum of ZnO, WO_3, and ZnO–WO_3 (5%, 10%, 15%, 20%) (a), Bandgap structure of all photoanodes (b)

Figure. 16(a) shows the valence band position construction using the XPS survey spectra for binding energies ranging from −3 to 6 eV. The estimated valence band position of ZnO nanosheets is 2.59 eV, that of WO_3 nanosheets is −0.55 eV, and that of ZnO–WO_3 hybrid NCs at different WO_3 contents 5, 10, 15, and 20 wt.% are 1.95, 1.77, 2.44, and 2.15 eV, respectively (**Figure. 16(b)**). When energy is absorbed that exceeds the bandgap of the semiconductor, electrons in the valence band (VB) are excited, whereas holes remain in the VB. These holes participate in water oxidation to produce O_2. To facilitate water splitting, the VB potential must exhibit a more positive value than the redox potential of O_2/H_2O, which is equivalent to 1.23 eV. The incorporation of WO_3 in ZnO negatively shifts the valence position in the ZnO–WO_3 hybrid NCs.

3.6. Photoluminescence emission behavior of ZnO–WO_3 hybrid NCs

Photoluminescence (PL) emission spectroscopy is more sensitive than normal optical absorbance to localized states induced by interfacial structural defects. The depth of these states within the forbidden gap can be determined by observing defect-related PL spectra arising from the recombination of trapped charge carriers with photogenerated holes [53]. In this study, the effect of interfacial hybridization between WO_3 and ZnO species in ZnO–WO_3 NCs at different WO_3 contents was monitored using PL emission spectra (**Figure. 17).**

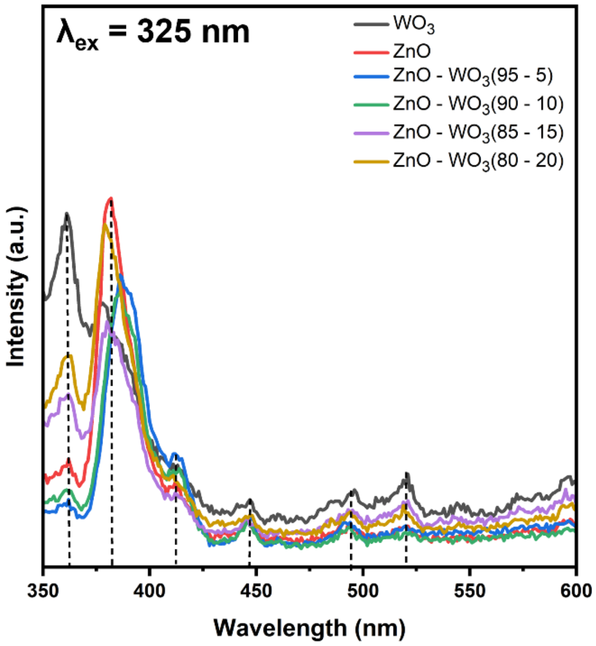

Figure 17. Photoluminescence emission spectra of ZnO NSs, WO_3 NSs, and ZnO–WO_3 hybrid nanocomposites at various WO_3 content.

The PL emission spectrum of ZnO NSs in **Fig. 17** at an excitation wavelength of 325 nm exhibited broad emission in the UV–visible spectral region [54], with observed emission peaks at 362, 382, 411, 445, 494, and 520 nm. The

UV emission bands at 362 and 382 nm were ascribed to fundamental band-edge emission and excitonic recombination [53,55]. The PL emission in the violet–blue spectra region at 411 and 445 was attributed to the trapped electrons recombining with photogenerated holes. These trapped electrons are located at shallow trapping levels, where they are linked to either interstitial zinc or oxygen vacancies [56]. The recombination of trapped electrons at deep trapping sites of single oxygen vacancies with photogenerated holes was mainly due to green emission around 520 nm [57–59]. Although the estimated optical bandgap of WO_3 NSs was lower than that of pure ZnO NSs (**Figure. 15(a, b))**, similar emission behavior was observed. The most intense UV emission band of the WO_3 NSs was observed at a lower wavelength of 362 nm than that of the ZnO NSs (378 nm). However, other emission bands were observed in the visible spectral range, covering violet (411 nm), blue (453 and 487 nm), and green (523 nm) emission bands [60]. The emission bands observed in the blue–green spectral region (453 and 487 nm) lie in the same energy range as the WO_3 bandgap (~2.6 eV). Therefore, they could be attributed to fundamental interband transitions [61–63]. The green emission observed at 523 nm occurred at an energy lower than the bandgap of $WO_{3,}$ which is ascribed to the recombination of trapped electrons in deep-localized oxygen vacancies with photogenerated holes [64]. Similar emission bands were observed in ZnO–WO_3 hybrid NCs at different WO_3 contents (5 w.%, 10 w.%, 15 w.%, and 20 w.%). Generally, the hybridization between ZnO and WO_3 led to a decrease in the PL emission intensity compared with the pure phases of ZnO and $WO_{3,}$ indicating quenching of the photogenerated carrier recombination rates. This behavior indicates an improvement in synergy hybrid NCs, which is accompanied by an improvement in photon energy conversion efficiency [15,65,66].

CHAPTER 4

PHOTOELECTROCHEMICAL WATER SPLITTING ANALYSIS

4.1. Photoelectrochemical water splitting measurements.

PEC water oxidation measurements were performed in a neutral medium of 0.5 M Na_2SO_4 for a modified FTO working electrode with ZnO nanosheets, WO_3 nanosheets, and a ZnO–WO_3 hybrid (NCs at various WO_3 contents (5 wt.%, 10 wt.%, 15 wt.%, and 20 wt.%). **Fig. 18(a)** shows the photocurrent response of all modified photoanodes in the potential range of 0–1.5 V vs. RHE (i.e., from −0.5 to 1 vs. Hg/HgO). The measured photocurrent ZnO–WO_3 NC hybrid photoanodes with WO_3 weight ratios of 5, 10, 15, and 20 wt.% were 66, 133, 38, and 31 μA, respectively. The obtained photoresponse current of hybrid ZnO–WO_3 NCs was higher than that of pure nanostructured phases of ZnO (18 μA) and WO_3 nanosheets (6 μA), demonstrating the improvement of photocurrent response compared with the pure phases as a result of the improved synergy between ZnO and WO_3 species in the hybrid NCs, which was accompanied by the enhancement of interfacial charge transfer at the electrode/electrolyte interface. The incident photon-to-current efficiency (IPCE) of the fabricated hybrid photoanodes at different polarization potentials was determined using the following **Equation (4)** [67]:

$$\mathrm{I}PCE(\%) \; = J_{ph}\frac{(1.23-(V- V_{OCP})}{P_{light}} \times \; 100\% \qquad (4)$$

where P_{light} is the incident power light density, J_{ph} is the photocurrent density, V is the polarization potential, and V_{OCP} is the change in the open-circuit potential (ΔOCP) under light (**Fig. 18(c))**. Achieving a higher open-circuit potential is crucial in PEC water splitting because it determines the maximum thermodynamic efficiency of the overall water-splitting process. In this study, ZnO–WO_3 NCs with 10 wt.% WO_3 hybrid photoanode achieved the highest open-circuit potential (OCP). Higher open-circuit potentials are important for optimal PEC cell operation [68,69]. **Fig. 18(b)** shows the potential-dependent IPCE(%), which is the calculated IPCE(%) value at 1.23 V vs. RHE (**Table 3)**.

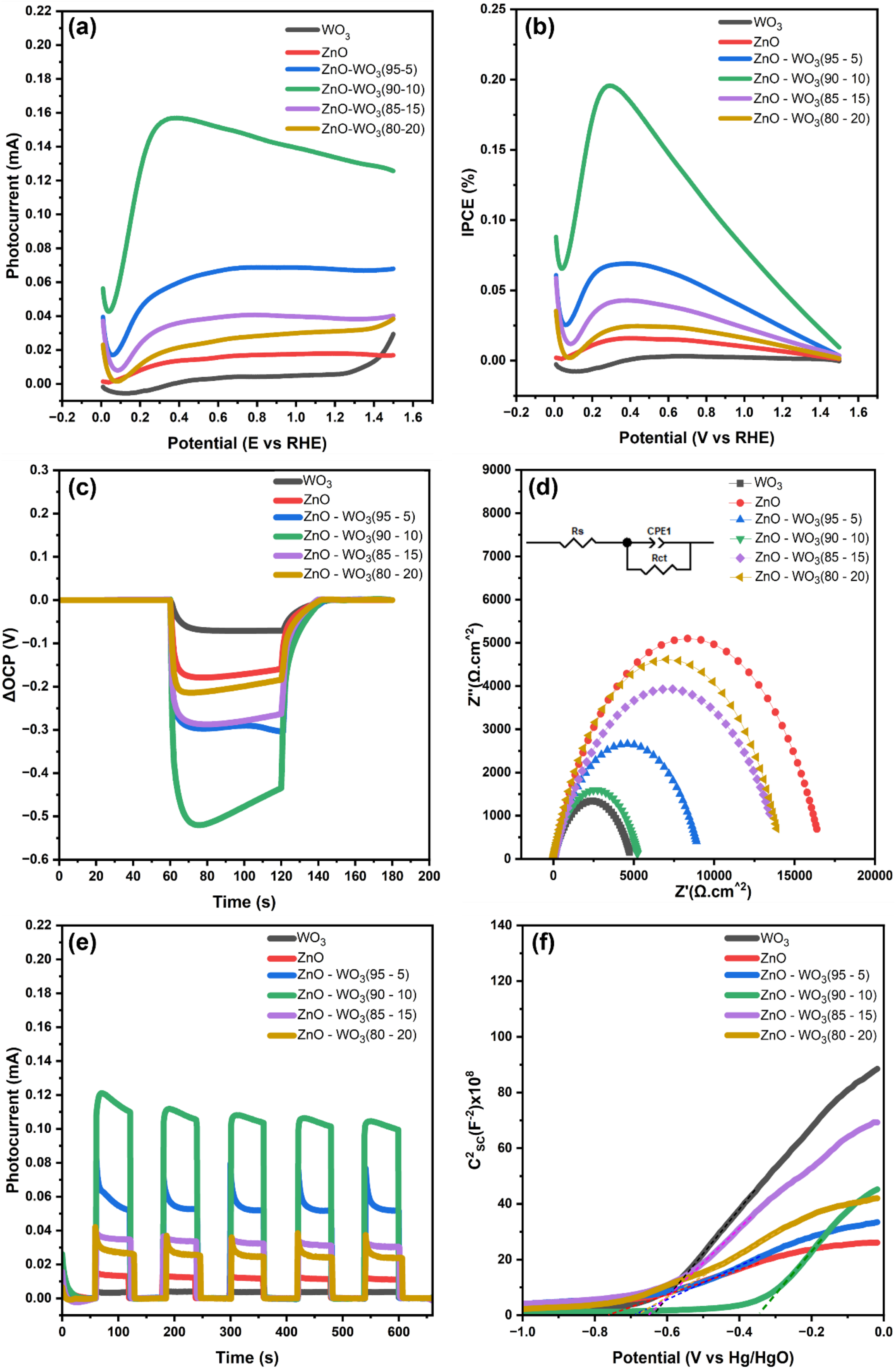
(a)
WO$_3$
ZnO
ZnO-WO$_3$(95-5)
ZnO-WO$_3$(90-10)
ZnO-WO$_3$(85-15)
ZnO-WO$_3$(80-20)
Photocurrent (mA)
0.00 0.02 0.04 0.06 0.08 0.10 0.12 0.14 0.16 0.18 0.20 0.22
−0.2 0.0 0.2 0.4 0.6 0.8 1.0 1.2 1.4 1.6
Potential (E vs RHE)
(b)
WO$_3$
ZnO
ZnO - WO$_3$(95 - 5)
ZnO - WO$_3$(90 - 10)
ZnO - WO$_3$(85 - 15)
ZnO - WO$_3$(80 - 20)
IPCE (%)
0.00 0.05 0.10 0.15 0.20 0.25
−0.2 0.0 0.2 0.4 0.6 0.8 1.0 1.2 1.4 1.6
Potential (V vs RHE)
(c)
WO$_3$
ZnO
ZnO - WO$_3$(95 - 5)
ZnO - WO$_3$(90 - 10)
ZnO - WO$_3$(85 - 15)
ZnO - WO$_3$(80 - 20)
ΔOCP (V)
−0.6 −0.5 −0.4 −0.3 −0.2 −0.1 0.0 0.1 0.2 0.3
0 20 40 60 80 100 120 140 160 180 200
Time (s)
(d)
Rs
CPE1
Rct
WO$_3$
ZnO
ZnO - WO$_3$(95 - 5)
ZnO - WO$_3$(90 - 10)
ZnO - WO$_3$(85 - 15)
ZnO - WO$_3$(80 - 20)
Z''(Ω.cm^2)
0 1000 2000 3000 4000 5000 6000 7000 8000 9000
0 5000 10000 15000 20000
Z'(Ω.cm^2)
(e)
WO$_3$
ZnO
ZnO - WO$_3$(95 - 5)
ZnO - WO$_3$(90 - 10)
ZnO - WO$_3$(85 - 15)
ZnO - WO$_3$(80 - 20)
Photocurrent (mA)
0.00 0.02 0.04 0.06 0.08 0.10 0.12 0.14 0.16 0.18 0.20 0.22
0 100 200 300 400 500 600
Time (s)
(f)
WO$_3$
ZnO
ZnO - WO$_3$(95 - 5)
ZnO - WO$_3$(90 - 10)
ZnO - WO$_3$(85 - 15)
ZnO - WO$_3$(80 - 20)
$C^2_{SC}(F^{-2})x10^8$
0 20 40 60 80 100 120 140
−1.0 −0.8 −0.6 −0.4 −0.2 0.0
Potential (V vs Hg/HgO)

Figure 18. Photoresponse current (a), incident photon conversion efficiency (b), difference in open-circuit potential (c), Nyquist plots under illumination (d) and chopped chronopotentiometry (e) at 1.23 V vs. RHE, and M–S plots (f) of ZnO–WO_3 NC photoanodes at various WO_3%.

Fig. 18(d) shows Nyquist plots of ZnO NSs, WO_3 NSs, and ZnO–WO_3 NC hybrid photoanodes under sunlight illumination at 1.23 V vs. RHE. The incorporation of WO_3 resulted in a reduction in the charge transfer resistance (Rct) of ZnO–WO_3 hybrid NCs compared with that of pure ZnO NSs, indicating an enhancement in the kinetics of interfacial charge transfer. To further assess the photoelectrochemical (PEC) capabilities, the Electrical Equivalent Circuit (EEC) model was analyzed for the fabricated photoanodes while being illuminated at 1.23 V_{RHE} (Fig 13(d)). The accompanying inset illustrates an RC circuit fitted to the data, with R_s representing solution resistance, R_{ct} denoting interfacial charge transfer resistance between the photoanode and electrolyte interfaces, and CPE as a constant phase element. Table 3 provides the calculated values of R_{ct}, Rs, and CPE based on the equivalent circuit scheme. The consistent R_s values of 10 Ω (±4 Ω) across all samples reflect stable solution conditions. However, the observed R_{ct} value of ZnO – WO_3(90 – 10) (5270 Ω) is markedly lower compared to ZnO and other nanocomposites. This lower R_{ct} for the ZnO – WO_3(90 – 10) interface indicates efficient separation of photogenerated electrons and holes in the photoanodes, attributed to the effective consumption of holes in the electrolyte solution. Furthermore, the semicircle diameter in the Nyquist plots represents the charge transfer behavior at the interfaces between the photoanodes and electrolytes. A smaller diameter signifies lower charge transfer resistance, indicating enhanced efficiency in the separation of photogenerated charge carriers. Similarly, the stability of the photoresponse current was validated for five complete cycles under dark and illumination states for all as shown, and hybrid photoanodes in **Fig. 18(e)**. The starting and ending frequency for the EIS measurement was 1000000 Hz & 0.001 Hz respectively for all electrodes. The peak intensity of the pure phases, WO_3 & ZnO frequencies of the Nyquist plot were 0.144 Hz, 0.077 Hz and the nanocomposites ZnO with (5, 10, 15, 20)% WO_3 frequency of the Nyquist plot was 0.078 Hz, 0.179 Hz, 0.067 Hz, 0.063 Hz. respectively.

Table 3. Equivalent-circuit fitting parameters including nussiance resistance (Rs), charge transfer resistance (Rct), and constant phase element (CPE) capacitance of ZnO–WO3 NC hybrid photoanodes at different WO3 contents.

Electrodes	**R_s (Ω)**	**R_{ct} (kΩ)**	**CPE (F)**
WO_3	8.34	4.82	0.00021
ZnO	10.97	16.76	0.000099
ZnO–WO_3 NCs (5 wt.% WO_3)	9.76	9.13	0.00017
ZnO–WO_3 NCs (10 wt.% WO_3)	11.43	5.27	0.00016
ZnO–WO_3 NCs (15 wt.% WO_3)	8.88	14.22	0.00017823
ZnO–WO_3 NCs (20 wt.% WO_3)	13.09	14.56	0.00016

Table 4. Photoresponse current (J_{ph}), incident photon conversion efficiency (IPCE), and charge transfer resistance (Rct) of ZnO–WO_3 NC hybrid photoanodes at different WO_3 contents.

Electrodes	**Photocurrent ($mA \cdot cm^{-2}$)**	**IPCE (%)**
WO_3	0.006	0.003
ZnO	0.018	0.016
ZnO–WO_3 NCs (5 wt.% WO_3)	0.066	0.069
ZnO–WO_3 NCs (10 wt.% WO_3)	0.133	0.196
ZnO–WO_3 NCs (15 wt.% WO_3)	0.038	0.043
ZnO–WO_3 NCs (20 wt.% WO_3)	0.031	0.025

Fig. 18(f) shows Mott–Schottky plots of ZnO NSs, WO_3 NSs, and ZnO–WO_3 NCs at various WO_3 contents (5%, 10%, 15%, and 20%), where the flat band potential (V_{fb}) and the corresponding donor density concentration (N_D) were estimated and recorded in **Table 4**.

$$\frac{1}{{C_{Sc}}^2} = \frac{1}{2\epsilon\epsilon_o e A^2 N_D}(V - V_{fb} - \frac{k_B T}{e}) \qquad (5)$$

where A is the electrode area, V is the applied potential, e is the electric charge of an electron, T is the absolute temperature, k_B is the Boltzmann constant, ϵ is the dielectric constant of ZnO (8.6) [15], and WO_3 (50) [70–72], ϵ_o is vacuum electric permittivity.

Table 5. Calculated donor concentration (N_D), flat band potential (V_{fb}), and width of the space charge layer (W_{scl}) of hybrid ZnO–WO_3 nanocomposite photoanodes across varying WO_3 content levels.

Electrode	V_{fb}	N_D x 10^{26}	W_{scl} **(nm)**
WO_3	−0.64	0.46	12.84
ZnO	−0.78	9.24	1.24
ZnO–WO_3 NCs (5 wt.% WO_3)	−0.69	6.70	1.42
ZnO–WO_3 NCs (10 wt.% WO_3)	−0.36	2.69	1.96
ZnO–WO_3 NCs (15 wt.% WO_3)	−0.65	4.06	1.79
ZnO–WO_3 NCs (20 wt.% WO_3)	−0.69	5.70	1.53

The combination of WO_3 with ZnO nanosheets increased the positive shift of V_{fb} for all hybrid photoanodes compared with photoanodes, which are composed solely of pure ZnO NSs. Compared to all hybrid photoanodes, the hybrid ZnO–WO_3 NCs containing 10 wt.% WO_3 exhibited the highest positive shift. The observed positive shift in V_{fb} indicates improved energy conversion efficiency [73]. However, the concentration of majority carriers (N_D) in n-type semiconductors by a direct route does not correlate with PEC cell performance. This is because N_D represents the concentration of charge carriers that do not participate in the PEC water-splitting reaction that occurs at the interface between the electrode and electrolyte. Despite this, alterations in N_D exert a substantial influence on the positioning of the Fermi level (E_f) concerning to the intrinsic energy level (E_i). This relationship is particularly relevant because (E_i) is situated at the center of the modified band structure of the electrode according to the following relationship:

$$E_f = E_i + KT \times \ln(\frac{N_D}{n_i}) \qquad (6)$$

Furthermore, the concentration of minority carriers (holes) within the space charge layer contributes to water oxidation and O_2 evolution during PEC water splitting. The space charge layer formed between the electrode, and electrolyte plays a significant role in the performance of energy conversion. According to K. Schwarzburg [74], the separation of photogenerated electron-hole pairs occurs rapidly within picoseconds in the depletion region because of an externally applied potential. In this process, electrons generated by light absorption relocate to the interior bulk area of the photoanode surface, while holes created in the process traverse toward the position between the electrode and electrolyte, contributing to the PEC water splitting process [75]. W_{scl} can be calculated using **Equation (7):**

$$W_{\mathrm{scl}} = \sqrt{\frac{2\epsilon\epsilon_o(V - V_{\mathrm{fb}})}{eN_D}} \qquad (7)$$

The calculated values for W_{scl} are shown in **Table 4**. Based on the calculated W_{scl} values, the photoanode ZnO–WO_3 (90–10) showed the highest value compared with the other hybrid photoanodes and pure ZnO/FTO. This explains why the incorporation of WO_3 content in ZnO at a certain limit (10%) enhances the charge kinetics of ZnO–WO_3 hybrid photoanodes and the concentration of photogenerated carriers within the space charge layer located at the interface between the electrode and electrolyte.

CHAPTER 5

CONCLUSION

ZnO–WO_3 NC hybrid photoanodes were deposited on an FTO substrate using a one-step dry NPDS process with no additional postprocess. The fabricated heterostructure electrodes were used to examine the PEC water splitting in a neutral electrolyte (0.5 M Na_2SO_4); SEM images clearly showed the microparticle transformation of nanosized structures in the deposited thin films. Raman spectra revealed a decrease in crystallinity due to kinetic-induced fragmentation in all hybrid photoanodes at WO_3 contents ranging from 5 to 20 wt.%. High-resolution XPS of the W 4f, Zn 2p, and O 1s bands revealed a negative shift with increasing ZnO content in the hybrid NCs, demonstrating improved interfacial synergy. Analysis of the diffuse reflectance spectra demonstrated that increasing the WO_3 to 10 wt.% reduced the ZnO bandgap from 3.24 to 3.20 eV in the hybrid photoanode. The PL emission spectra revealed that the ZnO with (10 wt.% WO_3) hybrid photoanodes showed the lowest emission intensity, indicating that the dissociation of photogenerated charges was improved. Analysis of Mott–Schottky plots across all hybrid photoanodes indicated a positive shift in the V_{fb} , reduction in N_D, and expansion of the space charge layer width compared with ZnO/FTO. This phenomenon exerted a substantial impact on the effective segregation of photogenerated electron-hole pairs within the space charge layer located at the interface between the electrode and electrolyte, leading to an overall enhancement in PEC water splitting. Note that the introduction of WO_3 into all hybrid heterostructure electrodes increased the photoresponse current and reduced the charge transfer resistance compared with nanoscale ZnO/FTO photoanodes. The ZnO–WO_3 NCs/FTO hybrid photoanodes with 5%, 10%, 15%, and 20% WO_3 content exhibited photocurrent of 0.066, 0.133, 0.038 and 0.031 $mA \cdot cm^{-2}$, respectively, compared with only 0.018 $mA \cdot cm^{-2}$ for pure ZnO/FTO and 0.006 $mA \cdot cm^{-2}$ for WO_3/FTO photoanodes at 1.23 V vs. RHE. Furthermore, the maximum IPCE for ZnO–WO_3 hybrid photoanodes exhibited a transition to a lower potential than that for ZnO/FTO and WO_3/FTO photoanodes. The ZnO–WO_3 hybrid photoanode with 10% WO_3 content revealed maximum efficiency of 0.196%. The stability of photocurrent for all NS photoanodes was validated for five cycles. Stability test revealed almost the same photocurrents. In contrast to alternative methods for fabricating hybrid ZnO–WO_3 nanocomposite photoanodes, the NC photoanodes in this study were fabricated in a very short time (**Table 5)** using only one-step dry NPDS method with commercially available microsized powders mixed with conventional ball milling. In addition, no additional postprocesses for binding, cleaning, or drying were required. Finally, 10% ZnO–WO_3 photoanode outperformed pure ZnO/FTO, WO_3/FTO, and other NC photoanodes in terms of PEC water splitting in a neutral electrolyte.

Table 6. The average consumable time for different material coatings in different techniques.

Coating Techniques	Material	Average Consumable Time (Hours)	Ref
Nanoparticle Deposition System (NPDS)	ZnO-WO_3	0.5	Our work
Sol-gel method+ Hummer's method	ZnO – Graphene Oxide	6.5	[76]
Aqueous chemical method	ZnO	11.3	[77]
Hydrothermal and cation exchange method	ZnO/$CuInS_2$	16	[78]
Solvothermal method	ZnO-WO_{3-x}	21	[79]

REFERENCES:

[1] A.J. Bard, M.A. Fox, Artificial Photosynthesis: Solar Splitting of Water to Hydrogen and Oxygen, Acc. Chem. Res. 28 (1995) 141–145. https://doi.org/10.1021/ar00051a007.

[2] K. Yuan, Q. Cao, X. Li, H.Y. Chen, Y. Deng, Y.Y. Wang, W. Luo, H.L. Lu, D.W. Zhang, Synthesis of WO3@ZnWO4@ZnO-ZnO hierarchical nanocactus arrays for efficient photoelectrochemical water splitting, Nano Energy. 41 (2017) 543–551. https://doi.org/10.1016/j.nanoen.2017.09.053.

[3] T. Nguyen, T. Thuy, S.K. Cho, Y. Amangeldinova, WO 3 – ZnO and CuO – ZnO nanocomposites as highly efficient photoanodes under visible light, (2020).

[4] S.S. Kalanur, L.T. Duy, H. Seo, Recent Progress in Photoelectrochemical Water Splitting Activity of WO3 Photoanodes, Springer US, 2018. https://doi.org/10.1007/s11244-018-0950-1.

[5] A.F. Palmstrom, P.K. Santra, S.F. Bent, Atomic layer deposition in nanostructured photovoltaics: tuning optical, electronic and surface properties, Nanoscale. 7 (2015) 12266–12283. https://doi.org/10.1039/c5nr02080h.

[6] D. Barreca, G. Carraro, A. Gasparotto, C. Maccato, T. Altantzis, C. Sada, K. Kaunisto, T.P. Ruoko, S. Bals, Vapor Phase Fabrication of Nanoheterostructures Based on ZnO for Photoelectrochemical Water Splitting, Adv. Mater. Interfaces. 4 (2017) 1–9. https://doi.org/10.1002/admi.201700161.

[7] Y. Chen, L. Wang, R. Gao, Y.C. Zhang, L. Pan, C. Huang, K. Liu, X.Y.

Chang, X. Zhang, J.J. Zou, Polarization-Enhanced direct Z-scheme ZnO-WO3-x nanorod arrays for efficient piezoelectric-photoelectrochemical Water splitting, Appl. Catal. B Environ. 259 (2019) 118079. https://doi.org/10.1016/j.apcatb.2019.118079.

[8] G. Wang, H. Wang, Y. Ling, Y. Tang, X. Yang, R.C. Fitzmorris, C. Wang, J.Z. Zhang, Y. Li, Hydrogen-treated TiO2 nanowire arrays for photoelectrochemical water splitting, Nano Lett. 11 (2011) 3026–3033. https://doi.org/10.1021/nl201766h.

[9] M. Mishra, D.M. Chun, α-Fe2O3 as a photocatalytic material: A review, Appl. Catal. A Gen. 498 (2015) 126–141. https://doi.org/10.1016/j.apcata.2015.03.023.

[10] K. Sivula, F. Le Formal, M. Grätzel, Solar water splitting: Progress using hematite (α-Fe 2O3) photoelectrodes, ChemSusChem. 4 (2011) 432–449. https://doi.org/10.1002/cssc.201000416.

[11] J. Su, L. Guo, N. Bao, C.A. Grimes, Nanostructured WO3/BiVO4 heterojunction films for efficient photoelectrochemical water splitting, Nano Lett. 11 (2011) 1928–1933. https://doi.org/10.1021/nl2000743.

[12] T. Zhu, M.N. Chong, E.S. Chan, Nanostructured tungsten trioxide thin films synthesized for photoelectrocatalytic water oxidation: A review, ChemSusChem. 7 (2014) 2974–2997. https://doi.org/10.1002/cssc.201402089.

[13] S. Palmas, P.A. Castresana, L. Mais, A. Vacca, M. Mascia, P.C. Ricci, TiO2-WO3 nanostructured systems for photoelectrochemical applications, RSC Adv. 6 (2016) 101671–101682. https://doi.org/10.1039/c6ra18649a.

[14] Y.S. Wudil, U.F. Ahmad, M.A. Gondal, M.A. Al-Osta, A. Almohammedi,

R.S. Sa’id, F. Hrahsheh, K. Haruna, M.J.S. Mohamed, Tuning of graphitic carbon nitride (g-C3N4) for photocatalysis: A critical review, Arab. J. Chem. 16 (2023). https://doi.org/10.1016/j.arabjc.2023.104542.

[15] A.G. Abd-Elrahim, D.M. Chun, Facile one-step deposition of ZnO-graphene nanosheets hybrid photoanodes for enhanced photoelectrochemical water splitting, J. Alloys Compd. 870 (2021) 159430. https://doi.org/10.1016/j.jallcom.2021.159430.

[16] P.M. Rao, L. Cai, C. Liu, I.S. Cho, C.H. Lee, J.M. Weisse, P. Yang, X. Zheng, Simultaneously efficient light absorption and charge separation in WO 3/BiVO4 Core/shell nanowire photoanode for photoelectrochemical water oxidation, Nano Lett. 14 (2014) 1099–1105. https://doi.org/10.1021/nl500022z.

[17] M.S. Kim, D.M. Chun, J.O. Choi, J.C. Lee, K.S. Kim, Y.H. Kim, C.S. Lee, S.H. Ahn, Room temperature deposition of TiO2 using nano particle deposition system (NPDS): Application to dye-sensitized solar cell (DSSC), Int. J. Precis. Eng. Manuf. 12 (2011) 749–752. https://doi.org/10.1007/s12541-011-0099-3.

[18] A. Galán-González, A.K. Sivan, J. Hernández-Ferrer, L. Bowen, L. Di Mario, F. Martelli, A.M. Benito, W.K. Maser, M.U. Chaudhry, A. Gallant, D.A. Zeze, D. Atkinson, Cobalt-Doped ZnO Nanorods Coated with Nanoscale Metal-Organic Framework Shells for Water-Splitting Photoanodes, ACS Appl. Nano Mater. 3 (2020) 7781–7788. https://doi.org/10.1021/acsanm.0c01325.

[19] J. Han, Z. Liu, Optimization and Modulation Strategies of Zinc Oxide-based Photoanodes for Highly Efficient Photoelectrochemical Water

Splitting, ACS Appl. Energy Mater. 4 (2021) 1004–1013. https://doi.org/10.1021/acsaem.0c02985.

[20] J. Zhang, G. Zhu, W. Liu, Y. Xi, D.A. Golosov, S. Zavadski, S.N. Melnikov, 3D core-shell WO3@α-Fe2O3 photoanode modified by ultrathin FeOOH layer for enhanced photoelectrochemical performances, J. Alloys Compd. 834 (2020) 154992. https://doi.org/10.1016/j.jallcom.2020.154992.

[21] Y. Xu, Q. Cao, Z. Yi, P. Wu, S. Cai, Adjusting the energy bands of WO3@ZnO nanocomposite heterojunction through the combination of WO3 thin film to improve its photoelectric performance, IEEE Access. 8 (2020) 171350–171358. https://doi.org/10.1109/ACCESS.2020.3024827.

[22] J. Ji, P. Sang, J.H. Kim, Improving the photoelectrochemical performance of spin-coated WO3/BiVO4/ZnO photoanodes by maximizing charge transfer using an optimized ZnO decoration layer, Ceram. Int. 47 (2021) 26260–26270. https://doi.org/10.1016/j.ceramint.2021.06.035.

[23] D.M. Chun, M.H. Kim, J.C. Lee, S.H. Ahn, A nano-particle deposition system for ceramic and metal coating at room temperature and low vacuum conditions, Int. J. Precis. Eng. Manuf. 9 (2008) 51–53.

[24] D.M. Chun, S.H. Ahn, Deposition mechanism of dry sprayed ceramic particles at room temperature using a nano-particle deposition system, Acta Mater. 59 (2011) 2693–2703. https://doi.org/10.1016/j.actamat.2011.01.007.

[25] D.M. Chun, J.O. Choi, C.S. Lee, S.H. Ahn, Effect of stand-off distance for cold gas spraying of fine ceramic particles (<5μm) under low vacuum and room temperature using nano-particle deposition system (NPDS), Surf. Coatings Technol. 206 (2012) 2125–2132.

https://doi.org/10.1016/j.surfcoat.2011.09.043.

[26] A.G. Abd-Elrahim, D.M. Chun, Fabrication of efficient nanostructured Co3O4-Graphene bifunctional catalysts: Oxygen evolution, hydrogen evolution, and H2O2 sensing, Ceram. Int. 46 (2020) 23479–23498. https://doi.org/10.1016/j.ceramint.2020.06.118.

[27] R. Yogamalar, R. Srinivasan, A. Vinu, K. Ariga, A.C. Bose, X-ray peak broadening analysis in ZnO nanoparticles, Solid State Commun. 149 (2009) 1919–1923. https://doi.org/10.1016/j.ssc.2009.07.043.

[28] S.S. Kalanur, Y.J. Hwang, S.Y. Chae, O.S. Joo, Facile growth of aligned WO3 nanorods on FTO substrate for enhanced photoanodic water oxidation activity, J. Mater. Chem. A. 1 (2013) 3479–3488. https://doi.org/10.1039/c3ta01175e.

[29] A.G. Abd-Elrahim, D.M. Chun, Nanosized Co3O4–MoS2 heterostructure electrodes for improving the oxygen evolution reaction in an alkaline medium, J. Alloys Compd. 853 (2021) 156946. https://doi.org/10.1016/j.jallcom.2020.156946.

[30] M.M.M. Mohammed, A.G. Abd-Elrahim, D.M. Chun, One-step deposition of a Ni(OH)2-graphene hybrid prepared by vacuum kinetic spray for high energy density hybrid supercapacitor, Mater. Chem. Phys. 244 (2020) 122701. https://doi.org/10.1016/j.matchemphys.2020.122701.

[31] M.F. Daniel, B. Desbat, J.C. Lassegues, B. Gerand, M. Figlarz, Infrared and Raman study of WO3 tungsten trioxides and WO3, xH2O tungsten trioxide tydrates, J. Solid State Chem. 67 (1987) 235–247. https://doi.org/10.1016/0022-4596(87)90359-8.

[32] J.Y. Zheng, G. Song, J. Hong, T.K. Van, A.U. Pawar, D.Y. Kim, C.W. Kim,

Z. Haider, Y.S. Kang, Facile fabrication of WO3 nanoplates thin films with dominant crystal facet of (002) for water splitting, Cryst. Growth Des. 14 (2014) 6057–6066. https://doi.org/10.1021/cg5012154.

[33] J.Z. Ou, M.H. Yaacob, M. Breedon, H.D. Zheng, J.L. Campbell, K. Latham, J. Du Plessis, W. Wlodarski, K. Kalantar-Zadeh, In situ Raman spectroscopy of H2 interaction with WO3 films, Phys. Chem. Chem. Phys. 13 (2011) 7330–7339. https://doi.org/10.1039/c0cp02050h.

[34] A. Wolcott, T.R. Kuykendall, W. Chen, S. Chen, J.Z. Zhang, Synthesis and characterization of ultrathin WO3 nanodisks utilizing long-chain Poly(ethylene glycol), J. Phys. Chem. B. 110 (2006) 25288–25296. https://doi.org/10.1021/jp064777b.

[35] Y. Spectroscopies, Y. Shigesato, A. Murayama, T. Kamimori, K. Matsuhiro, Characterization of Evaporated Amorphous Wo 3 Films, Appl. Surf. Sci. 33 (1988) 811.

[36] J. Díaz-Reyes, R. Castillo-Ojeda, M. Galván-Arellano, O. Zaca-Moran, Characterization of WO3 thin films grown on silicon by HFMOD, Adv. Condens. Matter Phys. 2013 (2013). https://doi.org/10.1155/2013/591787.

[37] R.F. Zhuo, H.T. Feng, Q. Liang, J.Z. Liu, J.T. Chen, D. Yan, J.J. Feng, H.J. Li, S. Cheng, B.S. Geng, X.Y. Xu, J. Wang, Z.G. Wu, P.X. Yan, G.H. Yue, Morphology-controlled synthesis, growth mechanism, optical and microwave absorption properties of ZnO nanocombs, J. Phys. D. Appl. Phys. 41 (2008). https://doi.org/10.1088/0022-3727/41/18/185405.

[38] R. Zhang, P.G. Yin, N. Wang, L. Guo, Photoluminescence and Raman scattering of ZnO nanorods, Solid State Sci. 11 (2009) 865–869. https://doi.org/10.1016/j.solidstatesciences.2008.10.016.

[39] P. Sundara Venkatesh, V. Ramakrishnan, K. Jeganathan, Raman silent modes in vertically aligned undoped ZnO nanorods, Phys. B Condens. Matter. 481 (2016) 204–208. https://doi.org/10.1016/j.physb.2015.11.010.

[40] A. Souissi, A. Marzouki, A. Sayari, V. Sallet, A. Lusson, M. Oueslati, Origin of the Raman mode at 379 cm-1 observed in ZnO thin films grown on sapphire, J. Raman Spectrosc. 42 (2011) 1574–1577. https://doi.org/10.1002/jrs.2887.

[41] R. Georgekutty, M.K. Seery, S.C. Pillai, A highly efficient Ag-ZnO photocatalyst: Synthesis, properties, and mechanism, J. Phys. Chem. C. 112 (2008) 13563–13570. https://doi.org/10.1021/jp802729a.

[42] F. Decremps, J. Pellicer-Porres, A.M. Saitta, J.C. Chervin, A. Polian, High-pressure Raman spectroscopy study of wurtzite ZnO, Phys. Rev. B - Condens. Matter Mater. Phys. 65 (2002) 921011–921014. https://doi.org/10.1103/PhysRevB.65.092101.

[43] A. Khan, Raman Spectroscopic Study of the ZnO Nanostructures, J. Pakistan Mater. Soc. 4 (2010) 5–9. http://mrl.uop.edu.pk/JPMS/issues/jpms7/5-9 Raman Spectroscopic Study of the ZnO Nanostructures Aurangzeb Khan.pdf.

[44] M. Tayebi, A. Tayyebi, Z. Masoumi, B.K. Lee, Photocorrosion suppression and photoelectrochemical (PEC) enhancement of ZnO via hybridization with graphene nanosheets, Appl. Surf. Sci. 502 (2020) 144189. https://doi.org/10.1016/j.apsusc.2019.144189.

[45] V.A. Online, R. Luque, R. V Hadi, H. Salehzadeh, V. Moradi, A.R. Solymani, RSC Advances, (n.d.).

[46] A.J.E. Rettie, K.C. Klavetter, J.F. Lin, A. Dolocan, H. Celio, A. Ishiekwene,

H.L. Bolton, K.N. Pearson, N.T. Hahn, C.B. Mullins, Improved visible light harvesting of WO3 by incorporation of sulfur or iodine: A tale of two impurities, Chem. Mater. 26 (2014) 1670–1677. https://doi.org/10.1021/cm403969r.

[47] T. Thiyagarajan, V. Deivasigamani, M. Raj, C. Joseph, T. Dheivasigamani, B. Palanivel, M.S. Hamdy, M. Shkir, Facile synthesis and characterization of WO3/CuWO4 nanocomposites for the removal of toxic methylene blue dye, Korean J. Chem. Eng. 38 (2021) 952–965. https://doi.org/10.1007/s11814-021-0756-x.

[48] S. Ilican, M. Caglar, S. Aksoy, Y. Caglar, XPS studies of electrodeposited grown f-doped ZnO rods and electrical properties of p-Si/n-FZN heterojunctions, J. Nanomater. 2016 (2016). https://doi.org/10.1155/2016/6729032.

[49] S. Limwichean, N. Kasayapanand, C. Ponchio, H. Nakajima, V. Patthanasettakul, P. Eiamchai, G. Meng, M. Horprathum, Morphology-controlled fabrication of nanostructured WO3 thin films by magnetron sputtering with glancing angle deposition for enhanced efficiency photo-electrochemical water splitting, Ceram. Int. 47 (2021) 34455–34462. https://doi.org/10.1016/j.ceramint.2021.08.359.

[50] S. Xu, D. Fu, K. Song, L. Wang, Z. Yang, W. Yang, H. Hou, One-dimensional WO3/BiVO4 heterojunction photoanodes for efficient photoelectrochemical water splitting, Chem. Eng. J. 349 (2018) 368–375. https://doi.org/10.1016/j.cej.2018.05.100.

[51] K.C. Leonard, K.M. Nam, H.C. Lee, S.H. Kang, H.S. Park, A.J. Bard, ZnWO4/WO3 composite for improving photoelectrochemical water

oxidation, J. Phys. Chem. C. 117 (2013) 15901–15910. https://doi.org/10.1021/jp403506q.

[52] M. Bilal Tahir, K. Nadeem Riaz, A.M. Asiri, Boosting the performance of visible light-driven WO3/g-C3N4 anchored with BiVO4 nanoparticles for photocatalytic hydrogen evolution, Int. J. Energy Res. 43 (2019) 5747–5758. https://doi.org/10.1002/er.4673.

[53] A.A. Othman, M.A. Ali, E.M.M. Ibrahim, M.A. Osman, Influence of Cu doping on structural, morphological, photoluminescence, and electrical properties of ZnO nanostructures synthesized by ice-bath assisted sonochemical method, J. Alloys Compd. 683 (2016) 399–411. https://doi.org/10.1016/j.jallcom.2016.05.131.

[54] L. Saikia, D. Bhuyan, M. Saikia, B. Malakar, D.K. Dutta, P. Sengupta, Photocatalytic performance of ZnO nanomaterials for self sensitized degradation of malachite green dye under solar light, Appl. Catal. A Gen. 490 (2015) 42–49. https://doi.org/10.1016/j.apcata.2014.10.053.

[55] A.A. Othman, M.A. Osman, E.M.M. Ibrahim, M.A. Ali, Sonochemically synthesized ZnO nanosheets and nanorods: Annealing temperature effects on the structure, and optical properties, Ceram. Int. 43 (2017) 527–533. https://doi.org/10.1016/j.ceramint.2016.09.189.

[56] M. Mazhdi, J. Saydi, M. Karimi, J. Seidi, F. Mazhdi, A study on optical, photoluminescence and thermoluminescence properties of ZnO and Mn doped-ZnO nanocrystalline particles, Optik (Stuttg). 124 (2013) 4128–4133. https://doi.org/10.1016/j.ijleo.2012.12.068.

[57] A.A. Othman, M.A. Osman, E.M.M. Ibrahim, M.A. Ali, A.G. Abd-Elrahim, Mn-doped ZnO nanocrystals synthesized by sonochemical method:

Structural, photoluminescence, and magnetic properties, Mater. Sci. Eng. B Solid-State Mater. Adv. Technol. 219 (2017) 1–9. https://doi.org/10.1016/j.mseb.2017.02.013.

[58] H. Zeng, G. Duan, Y. Li, S. Yang, X. Xu, W. Cai, Blue luminescence of ZnO nanoparticles based on non-equilibrium processes: Defect origins and emission controls, Adv. Funct. Mater. 20 (2010) 561–572. https://doi.org/10.1002/adfm.200901884.

[59] A.J. Reddy, M.K. Kokila, H. Nagabhushana, R.P.S. Chakradhar, C. Shivakumara, J.L. Rao, B.M. Nagabhushana, Structural, optical and EPR studies on ZnO:Cu nanopowders prepared via low temperature solution combustion synthesis, J. Alloys Compd. 509 (2011) 5349–5355. https://doi.org/10.1016/j.jallcom.2011.02.043.

[60] A. Pancielejko, M. Rzepnikowska, A. Zaleska-Medynska, J. Łuczak, P. Mazierski, Enhanced visible light active WO3 thin films toward air purification: Effect of the synthesis conditions, Materials (Basel). 13 (2020). https://doi.org/10.3390/MA13163506.

[61] W. Hu, Y. Zhao, Z. Liu, C.W. Dunnill, D.H. Gregory, Nanostructural Evolution : From One-Dimensional Tungsten Oxide Nanowires to Three-Dimensional Ferberite Flowers, (2008) 5657–5665.

[62] K. Kato, Y. Uemura, K. Asakura, A. Yamakata, Role of Oxygen Vacancy in the Photocarrier Dynamics of WO3Photocatalysts: The Case of Recombination Centers, J. Phys. Chem. C. 126 (2022) 9257–9263. https://doi.org/10.1021/acs.jpcc.2c01662.

[63] I.M. Szilágyi, B. Fórizs, O. Rosseler, Á. Szegedi, P. Németh, P. Király, G. Tárkányi, B. Vajna, K. Varga-Josepovits, K. László, A.L. Tóth, P. Baranyai,

M. Leskelä, WO 3 photocatalysts: Influence of structure and composition, J. Catal. 294 (2012) 119–127. https://doi.org/10.1016/j.jcat.2012.07.013.

[64] J.H. Ha, P. Muralidharan, D.K. Kim, Hydrothermal synthesis and characterization of self-assembled h-WO3 nanowires/nanorods using EDTA salts, J. Alloys Compd. 475 (2009) 446–451. https://doi.org/10.1016/j.jallcom.2008.07.048.

[65] M. Wang, A. Kafizas, S. Sathasivam, M.O. Blunt, B. Moss, S. Gonzalez-carrero, C.J. Carmalt, Applied Catalysis B : Environmental ZnO / BiOI heterojunction photoanodes with enhanced photoelectrochemical water oxidation activity, Appl. Catal. B Environ. 331 (2023) 122657. https://doi.org/10.1016/j.apcatb.2023.122657.

[66] A.G. Abd-Elrahim, D.M. Chun, Room-temperature deposition of ZnO-graphene nanocomposite hybrid photocatalysts for improved visible-light-driven degradation of methylene blue, Ceram. Int. 47 (2021) 12812–12825. https://doi.org/10.1016/j.ceramint.2021.01.142.

[67] H.M. Chen, C.K. Chen, R.S. Liu, L. Zhang, J. Zhang, D.P. Wilkinson, Nano-architecture and material designs for water splitting photoelectrodes, Chem. Soc. Rev. 41 (2012) 5654–5671. https://doi.org/10.1039/c2cs35019j.

[68] J.Y. Jung, J.Y. Yu, J.H. Lee, Dynamic Photoelectrochemical Device with Open-Circuit Potential Insensitive to Thermodynamic Voltage Loss, J. Phys. Chem. Lett. 9 (2018) 5412–5418. https://doi.org/10.1021/acs.jpclett.8b02295.

[69] F. Finger, K. Welter, F. Urbain, F. Urbain, V. Smirnov, B. Kaiser, W. Jaegermann, Photoelectrochemical Water Splitting using Adapted Silicon Based Multi-Junction Solar Cell Structures: Development of Solar Cells

and Catalysts, Upscaling of Combined Photovoltaic-Electrochemical Devices and Performance Stability, Zeitschrift Fur Phys. Chemie. 234 (2020) 1055–1095. https://doi.org/10.1515/zpch-2019-1453.

[70] M. Yagi, S. Maruyama, K. Sone, K. Nagai, T. Norimatsu, Preparation and photoelectrocatalytic activity of a nano-structured WO3 platelet film, J. Solid State Chem. 181 (2008) 175–182. https://doi.org/10.1016/j.jssc.2007.11.018.

[71] Y. Liu, Y. Li, W. Li, S. Han, C. Liu, Photoelectrochemical properties and photocatalytic activity of nitrogen-doped nanoporous WO 3 photoelectrodes under visible light, Appl. Surf. Sci. 258 (2012) 5038–5045. https://doi.org/10.1016/j.apsusc.2012.01.080.

[72] W. Li, J. Li, X. Wang, J. Ma, Q. Chen, Photoelectrochemical and physical properties of WO3 films obtained by the polymeric precursor method, Int. J. Hydrogen Energy. 35 (2010) 13137–13145. https://doi.org/10.1016/j.ijhydene.2010.09.011.

[73] K. Gelderman, L. Lee, S.W. Donne, Flat-band potential of a semiconductor: Using the Mott-Schottky equation, J. Chem. Educ. 84 (2007) 685–688. https://doi.org/10.1021/ed084p685.

[74] K. Schwarzburg, F. Willig, Modeling of electrical transients in the semiconductor/electrolyte cell for photogeneration of charge carriers in the bulk, J. Phys. Chem. B. 101 (1997) 2451–2458. https://doi.org/10.1021/jp962726g.

[75] W. Zhang, D. Yan, K. Appavoo, J. Cen, Q. Wu, A. Orlov, M.Y. Sfeir, M. Liu, Unravelling Photocarrier Dynamics beyond the Space Charge Region for Photoelectrochemical Water Splitting, Chem. Mater. 29 (2017) 4036–

4043. https://doi.org/10.1021/acs.chemmater.7b00672.

[76] M. Ghorbani, H. Abdizadeh, M. Taheri, M.R. Golobostanfard, Enhanced photoelectrochemical water splitting in hierarchical porous ZnO/Reduced graphene oxide nanocomposite synthesized by sol-gel method, Int. J. Hydrogen Energy. 43 (2018) 7754–7763. https://doi.org/10.1016/j.ijhydene.2018.03.052.

[77] R. Lv, T. Wang, F. Su, P. Zhang, C. Li, J. Gong, Facile synthesis of ZnO nanopencil arrays for photoelectrochemical water splitting, Nano Energy. 7 (2014) 143–150. https://doi.org/10.1016/j.nanoen.2014.04.020.

[78] Y. Li, Z. Liu, Y. Wang, Z. Liu, J. Han, J. Ya, ZnO/CuInS2 core/shell heterojunction nanoarray for photoelectrochemical water splitting, Int. J. Hydrogen Energy. 37 (2012) 15029–15037. https://doi.org/10.1016/j.ijhydene.2012.07.117.

[79] Y. Chen, L. Wang, R. Gao, Y.C. Zhang, L. Pan, C. Huang, K. Liu, X.Y. Chang, X. Zhang, J.J. Zou, Polarization-Enhanced direct Z-scheme ZnO-WO3-x nanorod arrays for efficient piezoelectric-photoelectrochemical Water splitting, Appl. Catal. B Environ. 259 (2019) 118079. https://doi.org/10.1016/j.apcatb.2019.118079.